Quasi-optical system for the DESHIMA spectrometer

Master's thesis

by

Sjoerd Bosma

2017-08-21

TU Delft

THz Sensing Group

DESHIMA

Quasi-optical system for the DESHIMA spectrometer

Master's thesis

by

Sjoerd Bosma

This thesis work has been performed at the Terahertz Sensing Group, Department of Microelectronics, Faculty of Electrical Engineering, Computer Science and Mathematics of the Delft University of Technology, Delft, The Netherlands, in partial fulfillment of the requirements for the degree of Master of Science in Electrical Engineering. This work is to be defended in public on 2017-08-25. This thesis work has been supervised by dr. N. Llombart, dr. A. Endo and dr. O. Yurduseven.

The graduation committee consists of dr. N. (Nuria) Llombart and dr. A. (Akira) Endo (Faculty of Electrical Engineering, Mathematics and Computer Science, TU Delft) and dr. A. (Aurèle) Adam (Faculty of Applied Sciences, TU Delft).

TU Delft THz Sensing Group DESHIMA

Het komt allemaal goed,
je moet het alleen doen.

Acknowledgments

The professors and teachers of the courses I followed have always lectured with great enthusiasm and dedication. Asking them questions was never a problem, no matter how weird some of them sound in retrospect. For their excellent work as teachers and motivators, I would like to sincerely thank prof. Andrea Neto, dr. Nuria Llombart, dr. Daniele Cavallo and dr. Giorgio Carluccio. Hopefully, one day I too can be a true Spartan.

I want to thank my office roommates Alicia, Arturo, Cantika, Diego, Harshitha, Ralph and Zhengzheng for the good times we had and will continue to have. Leaving my house to come home in the office is possible thanks to you. I want to thank the rest of the Terahertz Sensing group for all the fun we had during trips, dinners, lunches, coffees, beers or simply in the hallway.

I would like to thank all contributors to the DESHIMA project in the Netherlands, Japan, Chile and elsewhere for their hard work and dedication. A special mention goes to Tai Oshima and Tetsuya Takekoshi from Japan who have ensured my warm optics design has now been manufactured!

My supervisors have been phenomenal. Nuria, you are possibly the busiest person I know and yet you always find time to help me out with my trivial issues. I am very grateful to have you as a supervisor. Your uncanny ability to immediately point out a multitude of flaws in my ostensibly well-thought-out reasoning is equally terrific and terrifying. Akira, I want to thank you for all the support, technical and moral, during my thesis work. You're a great teacher and I wish you the most of luck with the DESHIMA project. Ozan, you are the best. The moment I joined the group as a complete EM newbie, you took my hand and have guided me through the mystery. Every single day for a year you have helped me for an hour or more. I am deeply thankful.

To my friends, thank you for dragging me back into the "real world" after spending too much time in the office.

Finally, to my parents and brother. Thank you for always letting me make my own decisions and for your wide open arms when I come crawling back for help or guidance. I love you.

Sjoerd Bosma,
Delft, August 2017

Contents

Chapter 1: Introduction

1.1 Motivation

Luminous, distant, dusty, star-forming galaxies represent the most intense starbursts in the Universe, yet they are completely obscured in the optical region [1]. Only recent technological advancements in terahertz (THz) technology have made studying these sub-millimeter galaxies (SMGs) possible [2].

Such studies are performed by large-format submm cameras such as SCUBA-2 (10k pixels) [3] and A-MKID (25k pixels, under development) [4], which offer 2D surveys of the skies at THz frequencies. Redshift determination of SMGs identified in this way can then be done by ALMA, as demonstrated recently for gravitationally lensed SMGs in [5]. However, unambiguous redshift determination of these galaxies using only ALMA was possible in just 12 out of 26 investigated galaxies[1]. To determine the redshift of the galaxies in [5] the authors employed ALMA band 3 ($84 - 116$ GHz) requiring 5 scans per galaxy due to the narrow instantaneous bandwidth of ALMA (≈ 8 GHz). This makes such redshift surveys complex, time-consuming and expensive. Quick redshift determination of identified high-z SMGs with unknown redshifts thus presents a gap in available instrumentation. DESHIMA, an on-chip direct-detection astronomical spectrometer operating in the submm band, is being developed to fill this gap [6].

DESHIMA will host 500 superconducting microwave kinetic inductance detector (MKID) channels per pixel forming an on-chip filterbank which can be simultaneously read out. Multiple pixels (3-7) detecting signals in the frequency band of $240 - 720$ GHz will be implemented. The spectral resolution is $f/\Delta f = 500$, which corresponds to ≈ 1 GHz bandwidth. This is the FWHM bandwidth of carbon monoxide lines from SMGs in the operational band of DESHIMA [7]. The matched spectral resolution and broad bandwidth promise high effi-

[1] Correlating with different data sources, the authors managed to obtain redshifts of 23 galaxies.

ciency in detecting spectral lines from high-z SMGs with unknown redshifts. DESHIMA is planned for deployment at the Atacama Submillimeter Telescope Experiment (ASTE) [8] in Chile with a narrowband demonstrator ($326 - 368$ GHz) planned for October 2017.

Technologically, DESHIMA builds upon breakthroughs in (superconducting) integrated technology developed at the Delft University of Technology in association with the Netherlands Institute for Space Research (SRON). Key enabling technologies are the leaky lens antenna [9], microwave kinetic inductance detectors [10] and their highly-multiplexed readout [11] and the required superconducting niobium titanium nitride / aluminum thin films [12], which all have been demonstrated by the Delft/SRON collaboration at submm wavelengths [13]–[16].

1.2 State of the art

Several other groups are developing spectrometers similar to DESHIMA, notably SuperSpec [17] and Micro-Spec [18]. SuperSpec aims for the $200 - 510$ GHz band using lumped-element KIDs, as opposed to the $\lambda/4$ KIDs for DESHIMA. Micro-Spec will operate in the $450-650$ GHz band and uses superconducting microstrip transmission lines as phase shifters to create an on-chip grating. Compared to these instruments, the bandwidth of DESHIMA is larger.

For these applications, ultra-wideband quasi-optical system designs are required. High aperture efficiency of the telescope is a key performance indicator for such systems. In order to achieve high, constant aperture efficiency over the complete frequency band, it is desired to use frequency-independent optics and an antenna with a radiation pattern that shows minimal frequency dispersion.

To couple radiation efficiently to a telescope over a large bandwidth, frequency-independent optics have been proposed using imaging beam waveguides in [19], with an application to the Crawford Hill telescope. This optics concept has subsequently been applied for the Submillimeter Array (SMA) optics [20] and more recently to an improved optics design for the SMA [21]. These Gaussian beam [22] techniques have also been used in this work.

In the literature, some studies have shown high aperture efficiency operation over a large bandwidth. For example, it has been shown in [23] that Vivaldi antennas can provide frequency-stable radiation patterns over an octave of bandwidth and 50% aperture efficiency at a single frequency has been demonstrated [24]. They are typically used for a single-feed-

per-beam scenario aimed at reflectors with low F/D-ratios ($f_{\#}$).

The eleven antenna has shown 60% aperture efficiency over a decade of bandwidth [25]. However, the antenna has only been shown in the microwave region for reflectors with low $f_{\#}$, typically in the order of ≈ 0.6.

Corrugated [26], [27], spline-profile [28] and ridged-flared horns [29] are among the interesting works presented in the literature. In [26], the proposed bandwidth of the horns is limited to 1:1.5 and 3 dB variation of directivity is reported within this band. Recently, a corrugated horn design with an optical efficiency[2] higher than 80% has been shown in [30]. However, the proposed bandwidth is limited to 1:1.7. To facilitate fabrication at high frequencies, as an alternative to corrugated horns, a smooth-walled spline-profile horn was presented in [28]. The work proposes a similar bandwidth, 1:1.5, to the corrugated horns with a directivity variation of 2.5 dB. A ridged, flared horn with a constant optical efficiency of around 70% was demonstrated for a 1:6 bandwidth in [29]. However, the horn is suitable for reflectors with $f_{\#} < 1$.

Lens-antenna based designs have also been extensively studied in the literature since they can provide fully integrated solutions for detector systems. Recently, a coherent array of leaky slots coupled to a silicon lens was demonstrated in [31] with an optical efficiency of about 80% in a 1:3 bandwidth. However, this design requires a microstrip feeding line which could be challenging to fabricate at sub-mm wavelengths. A study with an optimized profile based on a multi-shell lens [32] has shown 78% optical efficiency over a 1:3 bandwidth. It is worth mentioning that in [32] the wideband performance is not limited by the lens itself but by the feed employed. Therefore the 1:3 bandwidth was achieved by using two different waveguide feeds. While both [31] and [32] show high optical efficiencies over a 1.5 octave bandwidth, they are both single-feed solutions aimed at low F/D-ratios.

A high, 1:3 bandwidth, constant aperture efficiency reflector feed in the sub-mm regime has not been demonstrated for large $f_{\#}$. The high $f_{\#}$ is required to enable multi-pixel operation with lower scan loss than low $f_{\#}$ reflectors [33].

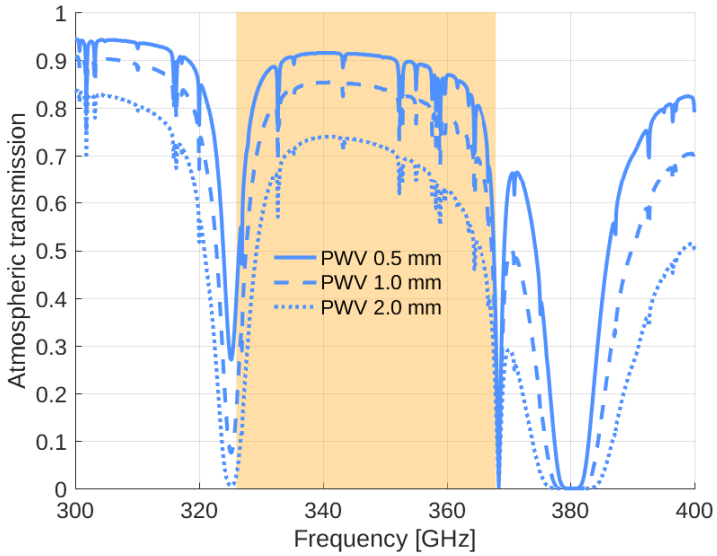

Fig. 1.1. Atmospheric transmission at the ASTE site as a function of frequency, for various levels of precipitable water vapor (PWV). The DESHIMA narrowband ($326 - 368$ GHz) is highlighted. The transmission has been calculated using http://www.apex-telescope.org/sites/chajnantor/atmosphere/transpwv/.

1.3 Narrowband system overview

In order to prove the viability of DESHIMA, a narrowband demonstrator ($326 - 368$ GHz) chip and quasi-optical system will be deployed on ASTE in October 2017. This frequency range corresponds to an atmospheric window in which the transmission of electromagnetic waves is high, see Fig. 1.1.

The DESHIMA spectrometer system consists of the following parts, shown schematically in Fig. 1.2:

- The 10 meter diameter telescope of ASTE and a 62cm diameter subreflector, in a Cassegrain setup, to couple THz radiation from the sky into the cabin. The measured surface roughness is below 18.9 μm [8]. The telescope is shown in Fig. 1.3a, with a cross-section shown in Fig. 1.3b and the pentagonal hole in the primary shown in Fig. 1.3c with $R_1 = 309$ mm and $R_2 = 250$ mm.

[2]Note that optical efficiency is called aperture efficiency in the referenced work. This excludes the radiation efficiency of the feed. In this thesis, aperture efficiency is the product of the optical efficiency and the radiation efficiency.

- Room-temperature optics (warm optics) located in the cabin of ASTE. The warm optics couple radiation from the telescope to the cold optics.
- A cryogenic cooler at $100\ \mathrm{mK}$, containing the on-chip spectrometer with integrated lens antenna, connected to a digital computer outside the cryostat to store measured data, and cold optics to couple incoming radiation from the warm optics to the antenna. The cryostat is shown in Fig. 1.4a and the spectrometer chip is shown in Fig. 1.4b.

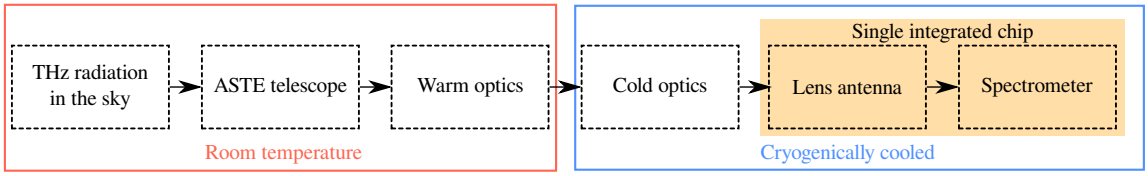

Fig. 1.2. Block-level overview of the DESHIMA spectrometer system.

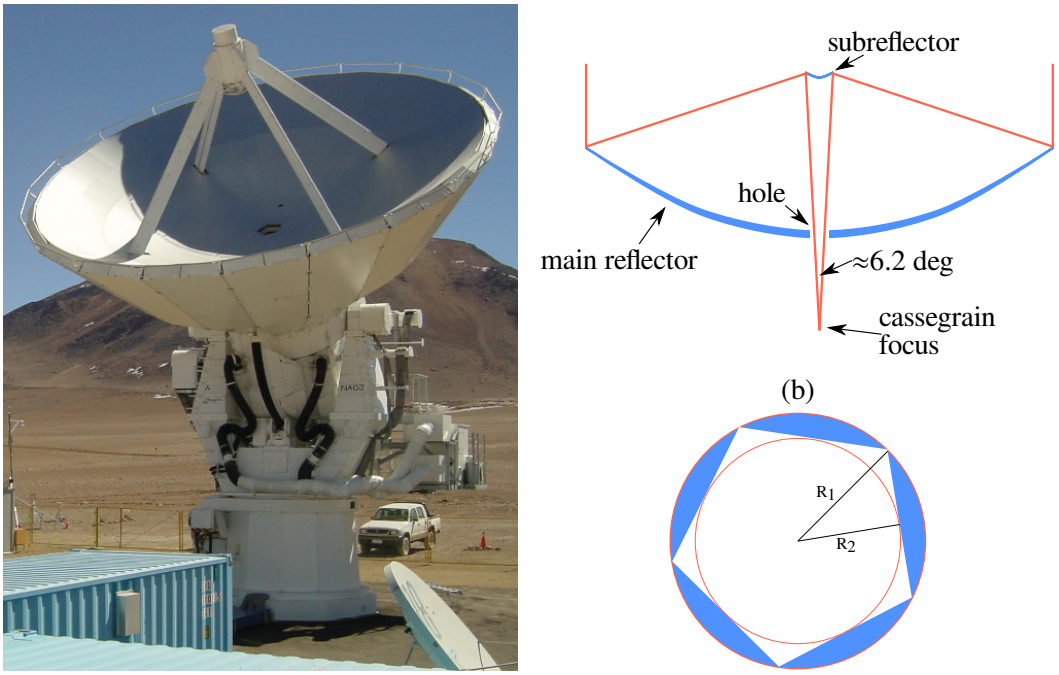

Fig. 1.3. (a) Photograph of the ASTE telescope in the Atacama desert, taken from http://www.ioa.s.u-tokyo.ac.jp/~kkohno/ASTE/. (b) Scale model with a side-view of the Cassegrain reflector and (c) the pentagonal hole of the telescope's main reflector.

The final wideband DESHIMA system is required to operate over the frequency band of $240 - 720\ \mathrm{GHz}$. The telescope must be illuminated with a tapered pattern to ensure

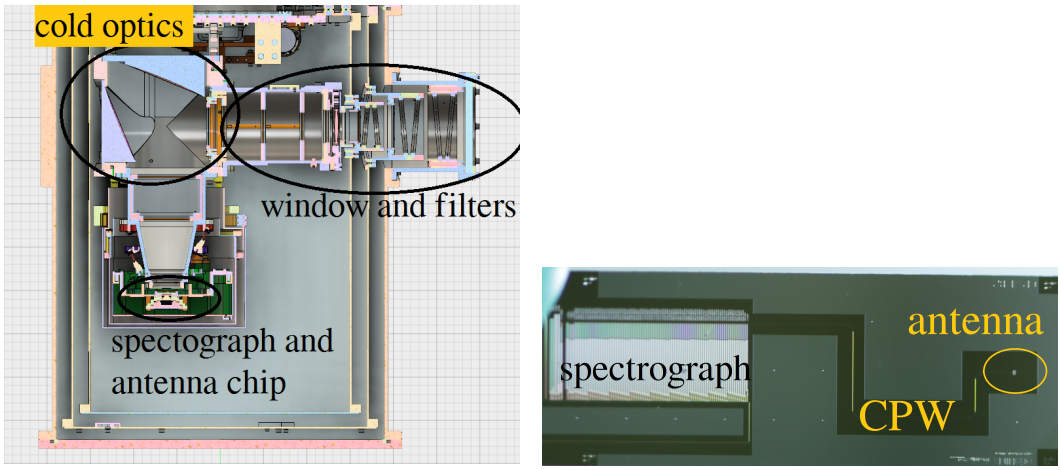

(a) (b)

Fig. 1.4. (a) Schematic drawing of the inside of the cryostat, indicating the window to the outside, the cold optics and the integrated spectrometer/antenna chip. (b) Close-up picture of the integrated spectrometer/antenna chip.

low sidelobes and low spill-over losses. A Gaussian distribution with a -11 dB edge taper leading to an aperture efficiency of 82% [22] is ideal. Good off-focus performance is required to facilitate multi-pixel operation. In Part II a preliminary investigation into the wideband antenna is made.

1.4 Existing baseline quasi-optical system

The quasi-optical system of the narrowband DESHIMA system consists of a narrowband antenna and a cold quasi-optical system, both inside a cryostat, and warm (room-temperature) quasi-optics placed in the cabin of ASTE.

At the start of this thesis work, the cold optics had been designed by S.J.C. Yates [34] of SRON. The evaluation of the performance of the double-slot lens antenna and cold optics using a PO approach with the real antenna patterns are presented in this thesis. The warm quasi-optical system had already been designed using a single-mode Gaussian optics approach [22]. During the evaluation of the warm quasi-optical system it was decided these optics were too complex, having three stand-alone mirrors. Additionally, multi-pixel operation was not possible due to a spill-over loss of 17 dB in the warm optics. Finally, the cryostat was re-positioned in the cabin of ASTE justifying the design of new warm optics. The design and

performance of the new warm optics is presented in this thesis.

1.5 Methodology

The results presented in this thesis have been obtained using the following analysis tools:

- 3D full-wave electromagnetic analysis for the double-slot lens antenna of Part I and the beams radiated into the dielectric by the leaky slot antennas of Part II using CST Microwave Studio (CST) [35]
- Physical optics (PO) based simulations using TICRA's GRASP software [36] to evaluate the performance of the quasi-optical system
- Ray-tracing software Zemax OpticStudio software [37] for tolerance analysis of the optical components.
- In-house developed PO tool to analyze lens antennas, detailed in [31], to analyze the leaky-lens antennas in Part II
- Self-implemented MATLAB routines to quantify efficiencies and perform preliminary designs.

The goal of this quasi-optical system is to achieve high aperture efficiency of the telescope's primary reflector, i.e. to effectively use the available area. The definitions of the efficiencies are given in Appendix B. Design and optimization of the warm optics is done through Gaussian models first. The quasi-optics are then evaluated using a PO analysis in GRASP to calculate the aperture efficiency using a Gaussian source. Then, the antenna's Gaussicity (or Gaussian coupling) is calculated. The multiplication of the aperture efficiency using a Gaussian source and the Gaussicity is a good indication for the overall aperture efficiency and has allows the optical system to be designed separately from the antenna. Once the quasi-optical system design is final, the aperture efficiency of the telescope is calculated by inputting the antenna radiation pattern as a source to the optics in GRASP.

The in-house developed PO tool to calculate the radiation from lens antennas [31] was used to evaluate the performance of the antennas in Part II. This tool is able to accurately calculate the radiation from lens antennas that are large in terms of wavelength.

The phase center of antennas were determined by evaluating the phase error loss over the -11 dB solid angle of the radiation pattern. This is described in Appendix A.

The efficiencies used in this thesis are as follows. The radiation efficiency, η_{rad}, of a (lens) antenna is the product of the front-to-back radiation efficiency, η_{F2B} and the reflection effi-

ciency η_{refl}. When coupled to a quasi-optical system, the spill-over efficiency of an antenna, η_{SO}, is the ratio of power intercepted by the system to the total power radiated by the antenna. The taper efficiency, η_{t} is the ratio of the directivity achieved by a quasi-optical system to the maximum theoretical directivity of the quasi-optical system. The optical efficiency, $\eta_{\text{opt}} = \eta_{\text{SO}}\eta_{\text{t}}$ is the product of the spill-over efficiency and the taper efficiency and reflects the beam quality of the antenna without taking into consideration its radiation efficiency. The aperture efficiency , η_{ap} is the ratio of achieved gain to the maximum theoretical directivity. Equivalently, this can be calculated as the product of all other efficiencies: $\eta_{\text{ap}} = \eta_{\text{rad}}\eta_{\text{opt}}$. The formulas used to calculate the efficiencies are given in Appendix B.

1.6 Thesis outline

This thesis consists of two parts. Part I describes the analysis of the narrowband DESHIMA quasi-optical system: the double-slot lens antenna in Chapter 2, an analysis of the cold quasi-optical system in Chapter 3, the design and analysis of a multi-pixel warm quasi-optical system in Chapter 4 and an analysis of the complete integrated quasi-optical system in Chapter 5. A conclusion of the narrowband system performance of Part I is given in Chapter 6.

Part II presents a preliminary analysis into a 1:3 bandwidth, integrated, leaky-lens antenna with frequency-stable radiation patterns with the aim of illuminating high-$f_{\#}$ reflectors. The selected antenna and lens designs are presented in Chapter 7. The performance of the lens antenna is evaluated using a simplified model of the quasi optical system of Part I. This simplified, equivalent quasi-optical system is presented in Chapter 8 along with the evaluation of the lens antenna's performance. A conclusion of Part II is given in Chapter 9.

Appendices A to E contain definitions of important parameters used in this thesis.

Part I
Narrowband quasi-optical system

Chapter 2: Double-slot lens antenna

This Chapter describes the analysis of the antenna under consideration, a double-slot antenna under an extended hemispherical dielectric lens. During the design of this antenna, a similar approach to the one in [38] has been followed, except for the material stratification used for the lens antenna. More precisely, instead of using a lens which is made of silicon only, this design has a thin wafer made of sapphire between the ground plane and the silicon lens [39]. The lens antenna geometry is fixed by DESHIMA project constraints and is further elaborated in Section 2.1 and the performance is evaluated in Section 2.2. The analysis in this Chapter is presented for $326, 350,$ and 368 GHz, the complete narrowband. A summary of the results can be found tabulated at the end of this Chapter, in Table 2.I.

2.1 Geometry

The considered lens-antenna design is shown in Fig. 2.1. It consists of a double-slot antenna under a dielectric lens. Using the design parameters in [38], the length of the slots is $0.28\lambda_{\text{air}}$ and the slot separation is $0.16\lambda_{\text{air}}$. The slots are etched in a superconducting niobium titanium nitride (NbTiN) ground plane which is characterized by a kinetic inductance of $1\ \text{pH}/\square$.

The dielectric lens, shown schematically in Fig. 2.1a, consists of a sapphire[1] wafer and an extended hemispherical lens made of silicon. The lens geometry is characterized by a radius $R = 4$ mm and extension $L = 0.39R = 1.56$ mm (including sapphire wafer). This extension length is known as a synthesized ellipse for silicon lenses, which is used to maximize the directivity of the secondary patterns. This is true when $R \gg \lambda_0$ [38]. This point will be addressed in Section 2.2. The sapphire wafer has a thickness $t = 0.35$ mm and the total height of the lens antenna is 5.56 mm. The lens is coated with a parylene ($\epsilon_r = 2.62$) matching layer with a thickness of $\lambda_{\text{ml}}/4 = 0.13$ mm.

[1] Sapphire is an anisotropic material with a relative permittivity of $\epsilon_{x,y} = 9.3$ and $\epsilon_z = 11.5$.

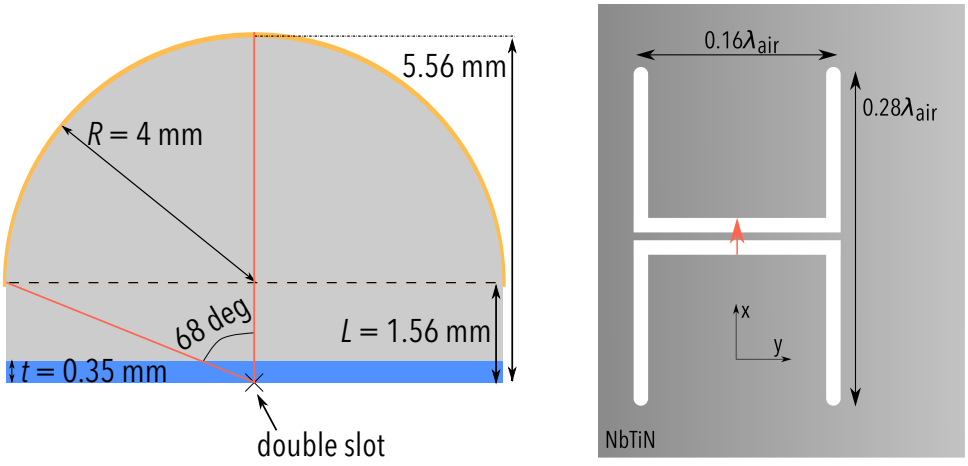

(a) (b)

Fig. 2.1. Geometry of the double-slot antenna (a) silicon (grey) lens on a sapphire (blue) wafer with parylene (orange) matching layer and (b) slot dimensions on the niobium titanium nitride ground plane.

2.2 Performance

The impedance matching of the double slot antenna has been calculated for the dielectric stratification given in Fig. 2.2a. In the calculation, the reference transmission line impedance is 82 Ω. The 82Ω was estimated to be the characteristic impedance of the co-planar waveguide connecting the antenna to the spectrometer, pictured in Fig. 1.4b. The resulting reflection coefficient is shown in Fig. 2.2b. The reflection coefficient over the frequency range $326 - 368$ GHz is below -13 dB, indicating excellent matching with 95% of the power transferred to the antenna.

The primary radiation patterns, i.e. the fields radiated inside the lens, were also evaluated using the stratification shown in Fig. 2.2a. The fields inside the lens are shown in Fig. 2.3. The field in the $\phi = 90$ deg is slightly more directive than the $\phi = 0$ or 45 deg planes, having its -10 dB value at 45 degrees compared to 50 degrees for the $\phi = 0$ and 45 deg cuts. Furthermore, the phase variation in the $\phi = 90$ deg cut is larger than in the $\phi = 0$ and 45 deg cuts. The maximum cross-polarization level is -11 dB in the $\phi = 45$ deg cut for $\theta = 60$ deg. It should be noted that any radiation in directions $\theta > 68$ deg, which corresponds to the region of the extension, does not contribute to far-field radiation outside the lens in broadside direction. This can be seen geometrically from Fig. 2.1a and constitutes

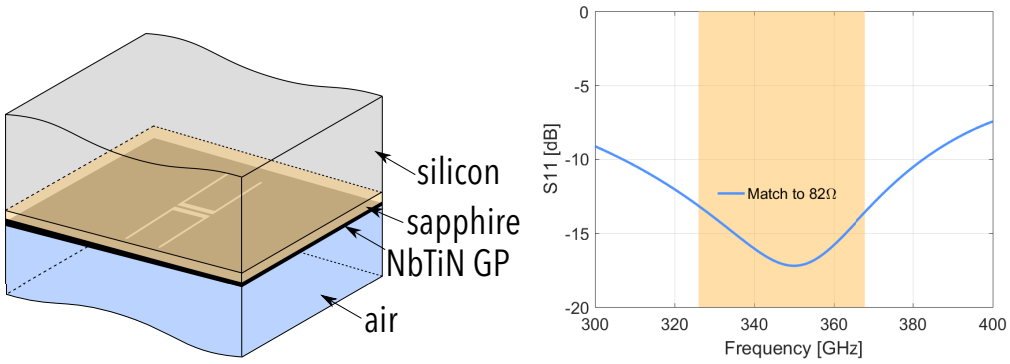

(a) (b)

Fig. 2.2. (a) Simplified stratification for the impedance and primary field calculation and (b) the resulting reflection coefficient normalized to a 82Ω load.

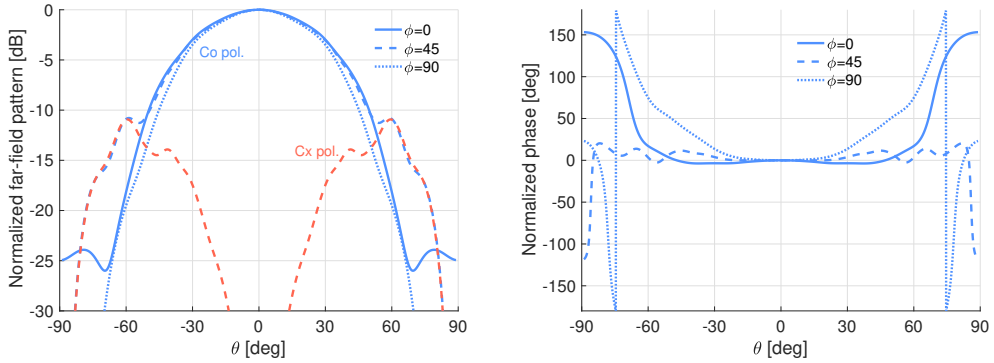

(a) (b)

Fig. 2.3. Primary radiation patterns of the double-slot antenna (a) amplitude and (b) phase.

spill-over loss. There is no simulated cross-polarization in the $\phi = 0$ or $\phi = 45$ deg cuts, as expected from a double-slot antenna.

The secondary radiation pattern, i.e. the field radiated outside the dielectric lens, and its phase distribution at 350 GHz are shown shown in Fig. 2.5. The -10 dB beamwidth varies from 5.5 deg for $\phi = 0$ deg to 6.8 deg for $\phi = 90$ deg. The maximum cross-polarization level has decreased to -18 dB which is observed for $\phi = 45$ deg. The phase efficiency (see Appendix A) of the lens antenna is maximized when the phase center is taken as the tip of the silicon lens, as shown in Fig. 2.4. The radiation patterns at 326 and 368 GHz, shown in Figs. 2.5c and 2.5d are practically the same, indicating frequency-stable radiation patterns over the complete narrowband range.

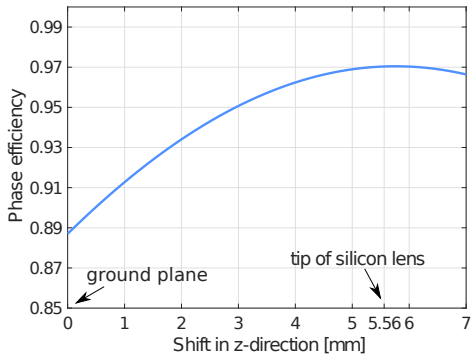

Fig. 2.4. Phase efficiency of the secondary patterns as a function of the far-field origin.

The expected directivity and Gaussicity for a silicon lens of this dimension are $30\ \mathrm{dBi}$ and 86%, respectively [38, Fig. 12]. The achieved values are significantly lower; the directivity is $28\ \mathrm{dBi}$ and the Gaussicity is 75%. This has two causes: First, the anisotropic sapphire causes significant widening of the beams when $\phi = 90\ \mathrm{deg}$, whereas the beams for a completely silicon lens would have more rotational symmetry. This is caused by the larger phase variation in the $\phi = 90\ \mathrm{deg}$ cut of the primary field. Second, as alluded to above, the lens extension length is not the optimum value to produce maximum directivity nor Gaussicity. Referring to [38, Fig. 13] gives an extension length of $L \approx 0.37R$ instead of the designed $L = 0.39R$ for $R/\lambda \approx 4.7$. Thus, the designed extension length is slightly larger than the optimum value and the double-slot antenna is no longer at the geometric focus of the synthesized ellipse.

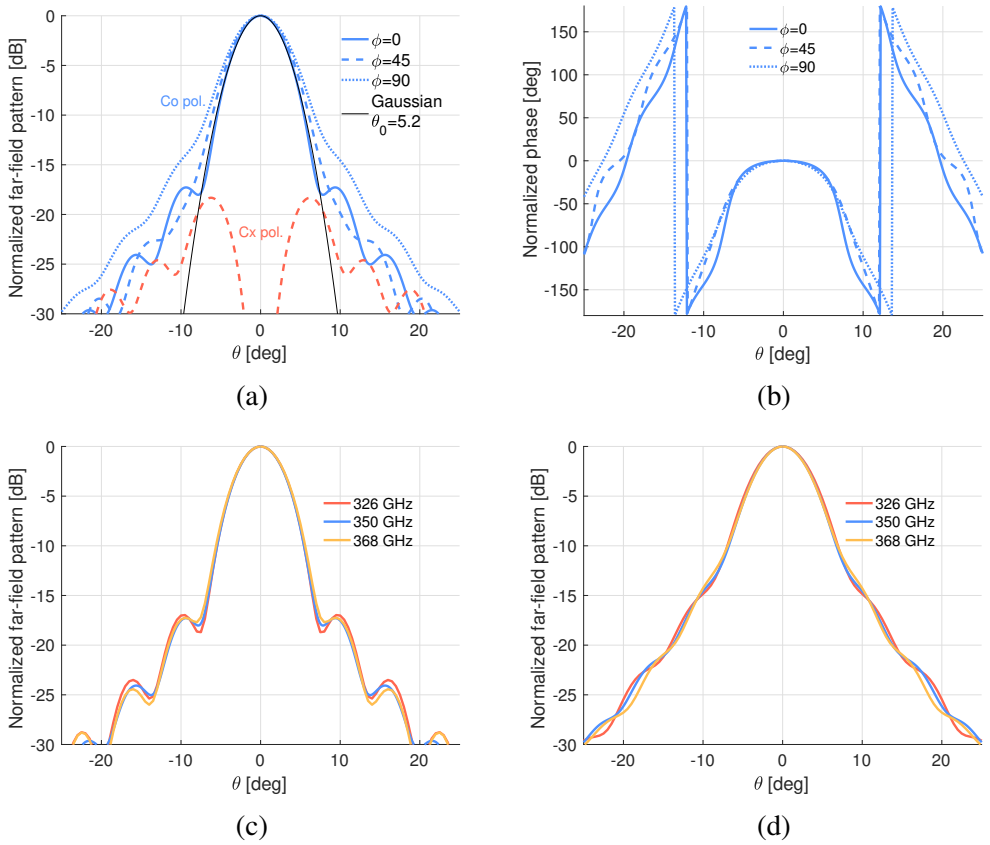

Fig. 2.5. Secondary radiation patterns of the double-slot antenna (a) amplitude and (b) phase at 350 GHz. A comparison of the co-polarized amplitudes over the frequency band $326 - 368$ GHz is shown for the cuts (c) $\phi = 0$ and (d) $\phi = 90$.

The radiation loss (see Appendix B) at 350 GHz of the lens antenna is 0.97 dB when the $\lambda/4$ parylene matching layer is present and 2.06 dB without the matching layer. Thus, the addition of a $\lambda/4$ matching layer reduces the radiation losses by more than 1 dB at the central frequency. According to [38, Fig. 11] the improvement should be around 1.6 dB. The lower improvement can be due to two reasons: First, in [38], the lens is made entirely of silicon without the effects of the anisotropic sapphire wafer that is included in the present work. Second, the parylene matching layer material ($\epsilon_r = 2.62$) does not have $\epsilon_r = \sqrt{11.9} \approx 3.45$ required for perfect matching between silicon and free space [40, p. 523].

The performance of the narrowband double-slot lens antenna is summarized in Table 2.I.

Table 2.I. Performance parameters of the double-slot lens antenna in the frequency band $326 - 368$ GHz.

Frequency [GHz]	326	350	368
Impedance mismatch loss [dB]	0.21	0.08	0.19
Radiation loss [dB]	1.27	0.97	1.08
Radiation loss (no ML) [dB]	-	2.1	-
Directivity [dBi]	27.8	28.0	28.0
Coupling to $\theta_0 = 5.2$ deg Gaussian [%]	76	75	75

2.3 Possible improvements

As discussed above, the performance of the lens-antenna is limited by the presence of the sapphire wafer and by the non-optimal lens extension length to synthesize an ellipse. Therefore, it was decided to investigate the improvements that could be gained by switching to a completely silicon design with an elliptical shape. The diameter of the lens was kept the same, to ensure the same physical space is taken up by the elliptical lens. The methodology described in [38] was used to design the lens. The double-slot antenna, exactly the same as used before, was positioned in the lower focus of the ellipse.

The secondary radiation patterns of the proposed silicon elliptical lens-antenna design are shown in Fig. 2.6a. Contrary to the secondary radiation patterns of the extended hemispherical lens of Fig. 2.5a, the main beam is symmetric in ϕ. Additionally the cross-polarization is 2 dB lower and the nulls are sharp for all ϕ-cuts. These effects combined result in a 1.2 dB increase in directivity and 12%-point higher Gaussicity to the same $\theta_0 = 5.2$ deg Gaussian. Furthermore, the radiation loss is 0.65 dB lower than for the lens with sapphire wafer. These results, summarized in Fig. 2.6b, match the expected directivity and Gaussicity from [38, Fig. 12].

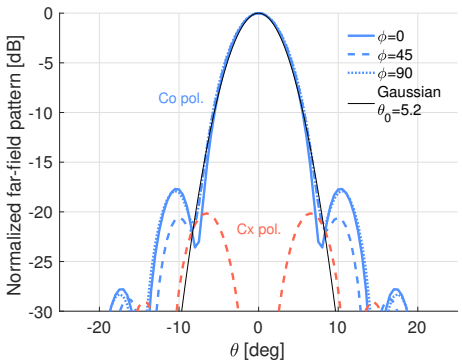

(a)

Frequency [GHz]	350
Radiation loss	0.32 dB
Directivity [dBi]	29.2
Coupling to θ_0 = 5.2 deg Gaussian [%]	87

(b)

Fig. 2.6. Proposed improved lens design (a) secondary radiation patterns and (b) performance parameters.

Chapter 3: Cold quasi-optical system

This Chapter describes the cryogenically cooled quasi-optical system, the cold optics, which is situated in the cryostat. The model used to simulate these optics has been designed by S.J.C. Yates [34] for an input Gaussian beam of $\theta_0 = 5.2$ deg and is detailed in Section 3.1. The performance obtained from these simulations is discussed in Section 3.2.

3.1 Geometry of the cold optics

The model of the cold optics consist of two offset parabolic mirrors and an aperture stop. The tip of the lens antenna of Chapter 2 is placed in the geometric focus of the first mirror (M1) which is a 45 deg offset paraboloidal mirror with a diameter of 92 mm and a focal length of 213 mm. The half-angle subtended by the lens antenna to the secondary mirror is approximately 12 deg. Rays propagating from the antenna to the secondary are then reflected to the second mirror (M2) which has the same focal length as the secondary but a slightly smaller diameter, 86 mm. M2 is also offset by 45 deg such that the central ray crosses itself perpendicularly. Stray light is blocked by a circular aperture stop with a diameter of 39 mm placed between the field lens and the parabolic mirrors. Geometrically, this aperture will block rays from the feed that exceed $\theta = 7$ deg. The filters and window of the cryostat shown in Fig. 1.4a are not included in the model.

3.2 Performance of the cold optics

To get an insight into how the aperture influences the radiation pattern after the focus, a Gaussian source with $\theta_0 = 5.2$ deg was used as an input to the cold optics. This Gaussian source has the highest coupling (75%) to the double-slot lens antenna and is a good model for the main beam of the lens antenna (see Chapter 2). The focal distances of M1 and M2

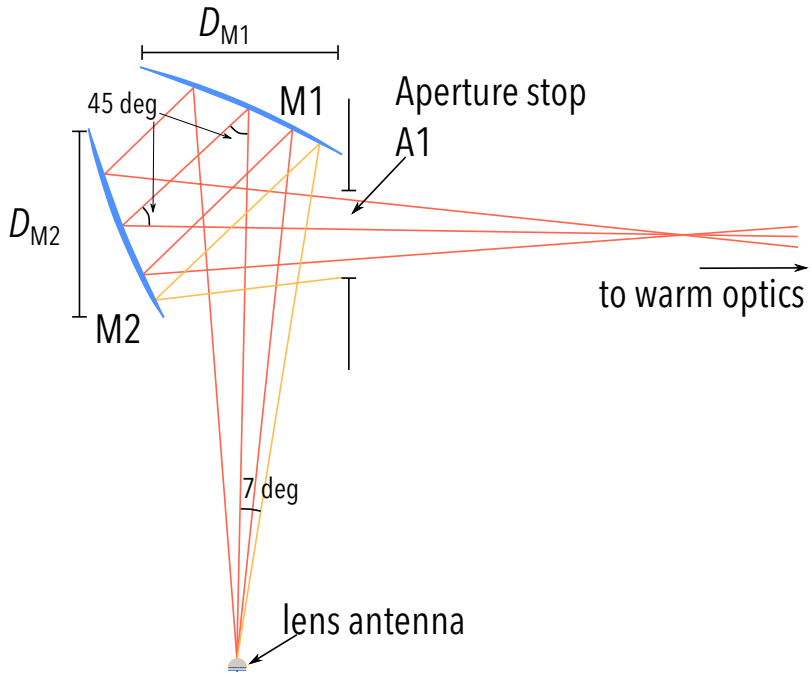

(a)

D_{M1}	92 mm
D_{M2}	86 mm
F_{M1}, F_{M2}	213 mm
$f_{\#\,M1}$	5.5
D_{A1}	39 mm

(b)

Fig. 3.1. (a) Schematic representation (to scale) of the cold optics. (b) Geometric properties of the cold optics.

are equal, meaning unity magnification in the cold optics. Thus, geometrically, the aperture stop influences angles $|\theta| > 7$ deg only. The field level of the Gaussian source at 7 deg is -15.7 dB and the aperture is expected to introduce a spill-over loss of 0.12 dB. Since the diffraction effects at this field level are almost negligible, the Gaussian input beam is expected to leave the cryostat the same as its feed pattern except for a truncation at $\theta > 7$ deg.

A PO simulation of the above scenario confirms the expectations. The input and output beams (symmetric in all ϕ-cuts) are shown in Fig. 3.2a. Only the region $\theta > 7$ deg is significantly affected: a more rapid decrease in field level can be seen due to the aperture. The same observations hold when the feed pattern is changed to the radiation pattern of the double-slot antenna of Chapter 2, shown in Fig. 3.2b: again only angles $\theta > 7$ deg are significantly affected. The field level for angles slightly below $\theta = 7$ deg are a little higher than before the aperture stop due to diffraction effects at the edges of the aperture stop. The maximum cross-polarization is reduced to -21 dB.

Next, the losses in the optics were assessed. These losses are caused by several effects: First, the antenna does not radiate all the power input at its terminals (radiation loss). Second,

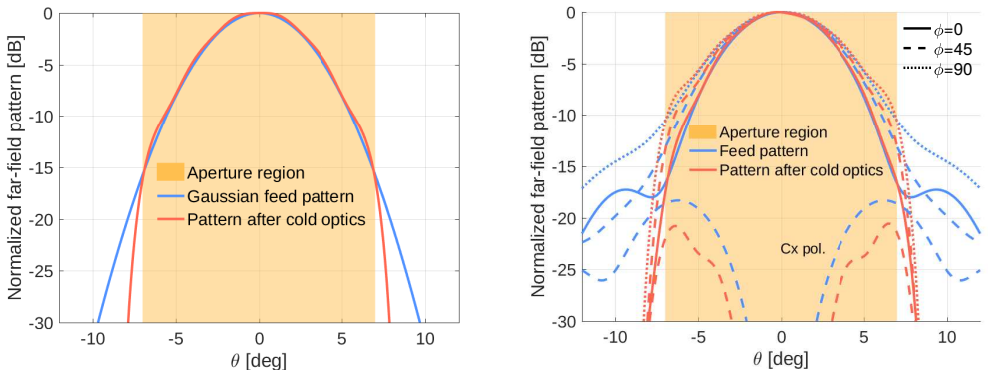

Fig. 3.2. Radiation patterns after the cold optics, shown for (a) a Gaussian source and (b) the double-slot lens antenna described in Chapter 2. The highlighted area is the geometrical angle for which the aperture is not obscuring any rays.

Table 3.I. Spill-over losses in the cold optics for the double-slot lens antenna in the frequency band $326 - 368$ GHz.

Element	**Losses [dB]**		
	326 GHz	350 GHz	368 GHz
Spill over M1	0.96	1.01	1.03
Spill over M2	0.06	0.06	0.05
Spill over A1	0.37	0.37	0.36
Cold spill over	1.39	1.44	1.44

the optical elements have finite size, leading to spill-over losses. This effect is also significant in the aperture, whose goal it is to block stray light, but has the secondary effect of obscuring part of the desired radiation.

The spill-over losses per element of the cold optics with the double-slot lens antenna feed are shown in Table 3.I for the frequency range of the DESHIMA narrowband demonstrator. At the central frequency, the total loss is 1.44 dB. The total cold spill-over loss increases slightly with frequency due to the decreasing front-to-back radiation efficiency of the double-slot lens antenna. The spill-over loss on M1 is high at all frequencies, but this is due to the front-to-back radiation ratio of the antenna.

The magnification is unity, as designed. The losses are dominated by the antenna design, not by the optical components which have low losses. Overall, the performance of the cold quasi-optical system is good.

Chapter 4: Warm quasi-optical system

This Chapter describes the design and performance evaluation of the room-temperature quasi-optical system, the warm optics, which are to be placed in the ASTE cabin. The role of the warm optics is to couple radiation from the telescope to the cold optics described in Chapter 3.

As we have seen in Section 1.4, the performance of the previous warm optics was unsatisfactory mainly because of high spill-over losses for offset pixels and the number of mirrors making the alignment of the optics more difficult and tolerance uncertain. Therefore, it was decided to redesign the optics. The cryostat was positioned more favorably: the optical axes of the teqlescope and cryostat now make a $90\ \mathrm{deg}$ angle.

With the optics still to be designed, many degrees of freedom were available. However, there were also some constraints and requirements. First, the warm optics must fit into the cabin of the telescope. Second, the warm spill-over losses must be low, meaning the optical components must be large with respect to the beamwidth after the cold optics. Third, support for multiple pixels is required with low scan losses for a $2\lambda_0 f_\#$ offset pixel. Finally, since the telescope cabin is a relatively cramped area where alignment of the warm optics might be difficult, tolerances on the positions of the mirrors are required.

4.1 Multi-pixel quasi-optical design

To simplify the first-order design, the warm optics were designed using the Gaussian beam approximation at the input. In this way, the magnification of the optics is $\mathcal{M} = \omega_{0,\mathrm{out}}/\omega_{0,\mathrm{in}} = \theta_{0,\mathrm{in}}/\theta_{0,\mathrm{out}}$ [22, Eq. 3.32]. The warm optical design can then be subjected to more rigorous analysis, for example by using physical optics, and small adjustments can then be made to iterate to the desired result.

The telescope subreflector subtended half-angle is $3.1\ \mathrm{deg}$ (Fig. 1.3b), and for maximum

aperture efficiency ($\approx 80\%$) we should illuminate this with an edge taper of -10.9 dB [22, Fig. 6.6]. This leads to a Gaussian beam with $\theta_{0,\text{out}} = 2.83$ deg. Since the output of the cold optics couples maximally to a $\theta_0 = 5.2$ deg Gaussian beam, we have $\theta_{0,\text{in}} = 5.2$ deg and the system magnification should be $\mathcal{M} = 1.84$. Note that we analyze the warm optics in transmission, meaning the input to the warm optics is the output of the cold optics and the output of the warm optics is the input to the telescope secondary.

Three optical layouts were considered: a single offset ellipsoidal reflector, a dual offset paraboloid layout like the the cold quasi-optical system and a modified Dragonian reflector system, the original being introduced in [41]. The modification consists of changing the paraboloid primary reflector to an ellipsoidal reflector which is almost identical but focuses not at infinity but at a real point closer to the main reflector.

The single offset (ellipsoidal) reflector is known to introduce cross-polarization [42], [43]. On the other hand, symmetric ellipsoidal reflectors have a larger field of view than dual-reflector systems at the same F/D ratio [44]. For the DESHIMA warm optics, a very large field of view is not required and the depolarization counts against the single ellipsoid as a solution.

The dual paraboloid setup has a smaller field of view than the ellipsoid, but in a compensated design (i.e. one where the Mizugutch condition is satisfied) the cross-polarization of one reflector is negated by the second, meaning this setup does not introduce additional cross-polarization [45]. A dual-paraboloid setup angled at 45 deg to each other satisfies this Mizugutch condition. However, the magnification achieved by such a system is the ratio of the focal lengths of the paraboloids: $\mathcal{M} = f_2/f_1$. Using, as a first estimate, the ratio of the vertical and horizontal path lengths in the cabin as the focal distances results in $\mathcal{M} \approx 3$. This magnification is too large for the system under consideration and the adjustment of the vertical or horizontal path lengths to justify the choice for a dual offset paraboidal mirror setup is not physically realizable within the constraints of the cabin space. Therefore, the dual offset paraboloid reflector concept is dismissed as a solution for the warm optics.

The classical Dragonian system has a field of view that is smaller than the field of view of a single symmetric ellipsoid [44]. However, the Dragonian is the dual reflector configuration that has the largest field of view [44]. Furthermore, the cross-polarization of a classical Dragonian setup can be as low as -60 dB [46]. Additionally, when the paraboloid primary reflector of the classical Dragonian is substituted with an ellipsoid, the magnification of this modified Dragonian can be tuned by changing the shape of the primary reflector without

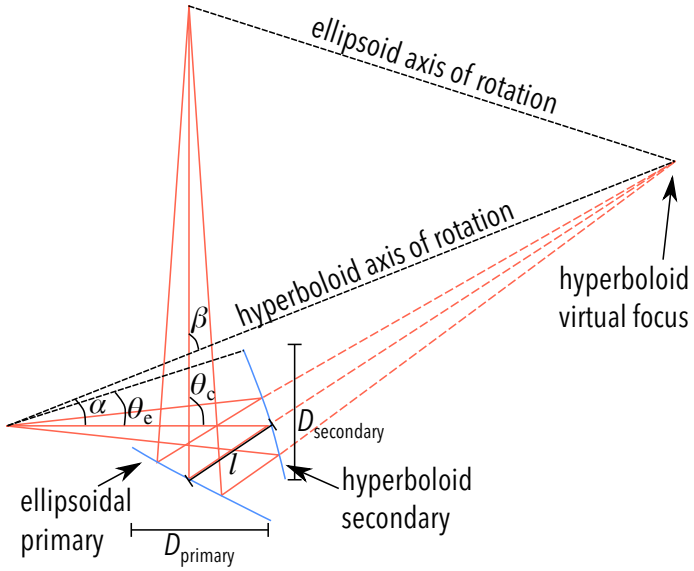

(a)

D_{primary}	320 mm
$D_{\text{secondary}}$	310 mm
θ_e	15 deg
α	-25 deg
β	-65 deg
l	260 mm
$\mathcal{M}$ (GO)	1.89

(b)

Fig. 4.1. (a) Schematic representation of the Dragonian warm optics design and (b) its geometric defining parameters. Further elaboration of the Dragonian system can be found in Appendix D.

changing its position. Therefore, a large range of magnifications is achievable with a compact geometry. For these reasons the modified Dragonian setup was investigated further.

Using the design guidelines in [46] for the side-fed type Dragonian with an ellipsoidal primary mirror, the configuration shown in Fig. 4.1a and tabulated in Fig. 4.1b was found. This modification of the Dragonian system was proposed in [33]. The geometrical magnification of this design is $\mathcal{M} = 1.9$ (a derivation of the geometrical-optics magnification is provided in Appendix D).

The diameter of both reflectors is a free parameter: they can be increased as long as they follow the curvature described by the hyperboloid or ellipsoid. A larger diameter leads to higher spill-over efficiency, but could also block the radiation intended to propagate to a different reflector. So, the size optimization is a compromise between spill-over efficiency and blockage. To determine the diameter, an analysis was done using Zemax with five pixels: a central pixel with four pixels surrounding this pixel in a square spaced at $2\lambda f_{\#} \approx 14$ mm, where λ was chosen at the lowest frequency for the wideband design discussed in Part II, 240 GHz, and $f_{\#} = 5.5$ is the f-number of the secondary reflector of the cold optics. The spill-over can then be traded-off against the blockage to determine the reflector diameters.

A refractive optical component is required to achieve $2\lambda f_{\#}$ scanning in the focal plane of the antenna. Without this component, an additional spill-over loss of 8.5 dB occurs on the telescope's secondary for offset pixels. This effect is shown by the black lines in the inset of Fig. 4.2. The best place for a refractive component is in one of the focal planes of the warm optics: here, the field of each pixel can be manipulated individually. The focal plane between the cold and warm optics was chosen as the location for the field lens, indicated in Fig. 4.2. This location is inside the cryostat. The focal plane between the warm optics and the telescope's secondary is not accessible since it is outside the ASTE cabin. An existing field lens design [34] served as a basis to fulfill the new design requirements.

Due to the size constraints in the cold optics, the maximum total thickness of the refractive field lens is 5 mm. Additionally, the diameter is limited to 40 mm. Using Zemax's optimization tool, a high-density polyethylene (HDPE, $\epsilon_r = 2.31$) was designed, shown in Fig. 4.3a. The field lens surface consists two conic surfaces, the second being the mirror image of the first in the xy-plane at $z = 2.5$ mm. The definition of the first conic surface is given in Appendix C with the parameters in Fig. 4.3b. The field lens was optimized for low spill-over loss on the telescope's secondary reflector for offset pixels. The reflections due to the air-dielectric interface at the field lens cause a spill-over loss of 0.37 dB.

4.2 Performance of the warm optics

The performance of the warm quasi-optical system was evaluated in GRASP by inputting a Gaussian source and determining the magnification, spill-over, level of cross-polarization introduced and possible asymmetries after the Dragonian system. The input beam is a 5.2 deg Gaussian beam that is symmetric around $\theta = 0$ deg. The output beam is a 2.75 deg Gaussian beam with negligible distortions and cross-polarization levels lower than -39 dB . This is higher than the -60 dB in [46] because an ellipsoidal primary is used here. The input and output beams are shown overlaid in Fig. 4.4a. The achieved magnification is $\mathcal{M} = 1.84$, very close to the geometric optics prediction. The small difference in the achieved output beam leads to a negligible loss ($< 1\%$-point) in aperture efficiency on the subreflector [22, Fig. 6.5].

The Strehl ratio in the focal plane of the telescope's secondary, calculated using Gaussian sources in the antenna focal plane with Zemax, is 1 for the central pixel and higher than 0.79 for a $2\lambda f_{\#}$ shift in the focal plane.

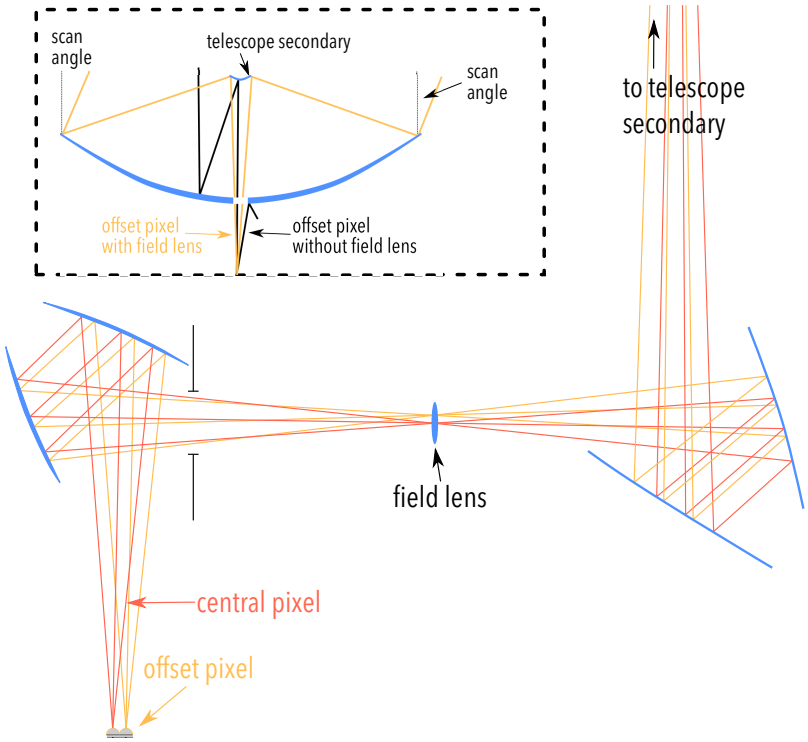

Fig. 4.2. Ray picture for two pixels in the focal plane of the cold optics (not to scale). The inset shows the spill-over loss that would occur on the telescope secondary in absence of the field lens.

4.3 Conclusion

After an analysis of various possible reflector setups, a modified Dragonian system was chosen for the warm quasi-optical system of DESHIMA. The two designed mirrors achieve the correct magnification, have a reasonable size and introduce low cross-polarization. Furthermore, the warm optics have been evaluated for four pixels surrounding the central pixel at a distance of $2\lambda f_{\#}$ in the antenna focal plane, for which the modified Dragonian also shows excellent performance after a field lens was introduced in the cold optics.

Mechanical design of the holders and adjustment mechanism for the mirrors has been performed by Tai Oshima and Tetsuya Takekoshi in Japan, where the mirrors will be manufactured too. A CAD rendering of the mirrors is shown in Fig. 4.5.

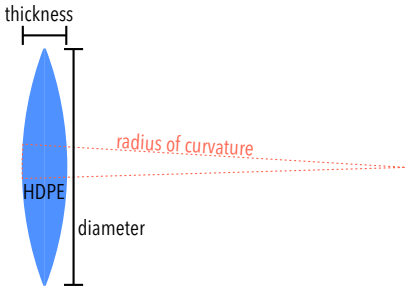

(a)

ϵ_r of HDPE	2.31
Field lens diameter	40 mm
Field lens conic const.	-0.658
Field lens rad. of curv.	95 mm
Field lens thickness	5 mm

(b)

Fig. 4.3. (a) Schematic cut of the field lens and (b) its defining parameters. The conic constant and a formula for the surface of the field lens are explained in Appendix C.

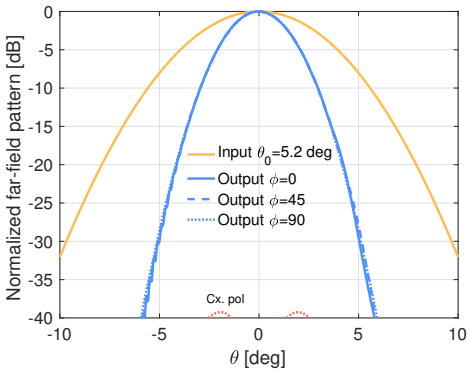

(a)

$\mathcal{M}$ (PO)	1.9
Max. cross-polarization	-39 dB
Strehl ratio central pixel	1
Strehl ratio offset pixel (min.)	0.79
Additional spill-over loss offset pixel (max.)	0.03 dB

(b)

Fig. 4.4. (a) Input-output relation of the warm optics and (b) other characteristics of the warm optics. The Strehl ratio and additional spill-over represent the worst-case offset pixels.

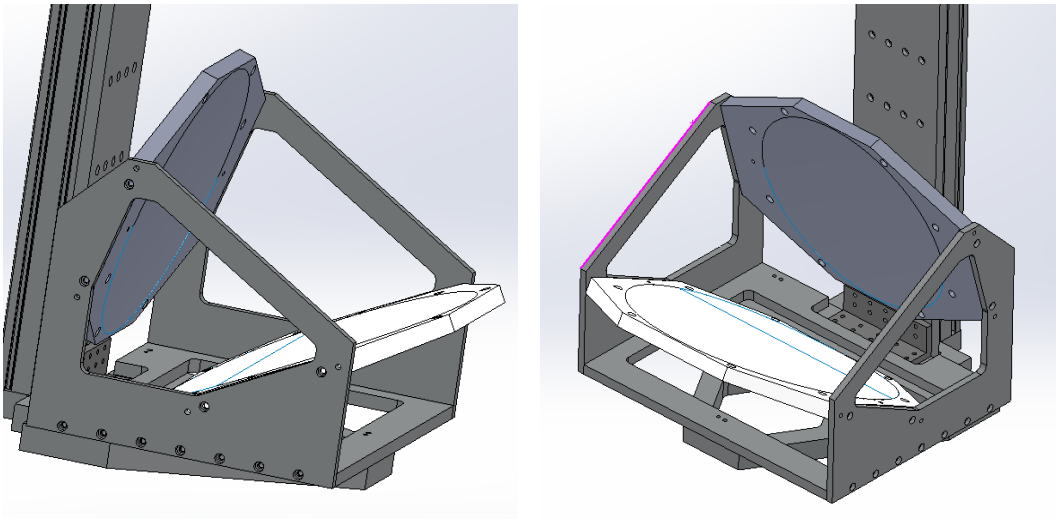

(a) (b)

Fig. 4.5. CAD drawing of the warm optics.The white mirror is the primary (ellipsoid) and the gray mirror is the secondary (hyperboloid). There is an elaborate support mechanism attaching the mirrors to the ceiling of the ASTE cabin.

Chapter 5: Performance of the quasi-optical system on ASTE

The performance of all quasi optics – cold, warm and telescope – of the DESHIMA narrow-band was analyzed using a PO approach. In Section 5.1, a Gaussian beam is used as feed to see only the influence of the optics. Then, in Section 5.2, the double-slot lens antenna of Chapter 2 is used as a feed. The main indicator of performance is the aperture efficiency of the telescope, explained in Appendix B. The patterns after the telescope are given, along with a table of efficiencies. The results of a tolerance analysis are given in Section 5.3.

5.1 Gaussian source as feed

A Gaussian beam with $\theta_0 = 5.2 \text{ deg}$ was used as a feed. This Gaussian beam is a good model for the double-slot antenna's main beam, as shown in Chapter 2. The radiation pattern of this feed after the telescope is shown in Fig. 5.1b. The radiation patterns are symmetric in all ϕ and the maximum side-lobe level is -26 dB. The maximum cross-polarization is lower than -40 dB.

After the telescope, the taper efficiency is 82% and the spill-over efficiency is 94%, resulting in an optical efficiency of 76%. This result proves the cascade of the cold optics, warm optics and telescope perform very close to the theoretical maximum aperture efficiency of 82%. This small difference can be explained by the illumination of the telescope's secondary reflector. The illumination is shown in Fig. 5.1a. For maximum optical efficiency the illumination should be -11 dB but the actual taper is -12.7 dB. Therefore, the spill-over efficiency is higher than 90% at the cost of a lower than 90% taper efficiency. The field lens reflections (FLR) cause another loss, leading to an aperture efficiency of 71% for the central pixel.

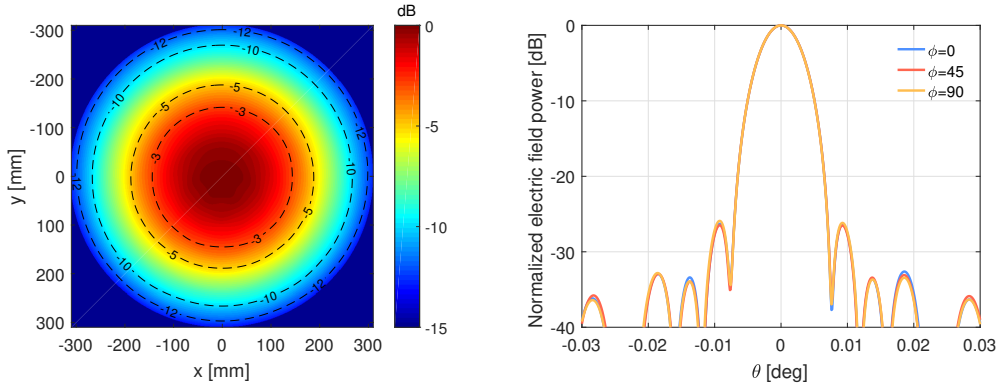

(a) (b)

Fig. 5.1. (a) Illumination of the telescope's secondary mirror and (b) radiation pattern after the telescope's primary mirror for a Gaussian beam source with $\theta_0 = 5.2$ deg.

The efficiencies, or equivalently the losses, are tabulated in Table 5.I.

5.2 Lens antenna as feed

The double-slot lens antenna of Chapter 2 was used as a feed into the complete quasi-optical system. The illumination of the telescope's secondary mirror is shown in Fig. 5.2a. In the $x = 0$ mm cut of the telescope's secondary, the illumination is similar to the Gaussian beam feed discussed above, -12.7 dB. In the $y = 0$ mm cut the edge taper is instead -8 dB, leading to higher spill-over loss in that plane. This asymmetry is due to the asymmetric radiation patterns of the antenna as discussed in Chapter 2.

The radiation pattern after the telescope's primary mirror is shown in Fig. 5.2. The maximum cross-polarization is -24 dB and is observed in the $\phi = 45$ deg cut. The maximum side-lobe level is -20.3 dB, but it differs in each plane due to the asymmetric illumination of the telescope's secondary, discussed above.

The aperture efficiency of the primary mirror of the telescope is 47% at 350 GHz. The spill-over efficiency is lower than for a Gaussian source due to the side lobes of the double-slot antenna and the higher edge illumination in the $y = 0$ mm cut. The taper efficiency is higher than for a Gaussian source due to the higher edge illumination in the $y = 0$ mm cut. The achieved maximum directivity is 90.68 dBi.

The aperture efficiencies of the central pixels at 326 GHz and 368 GHz are 48% and

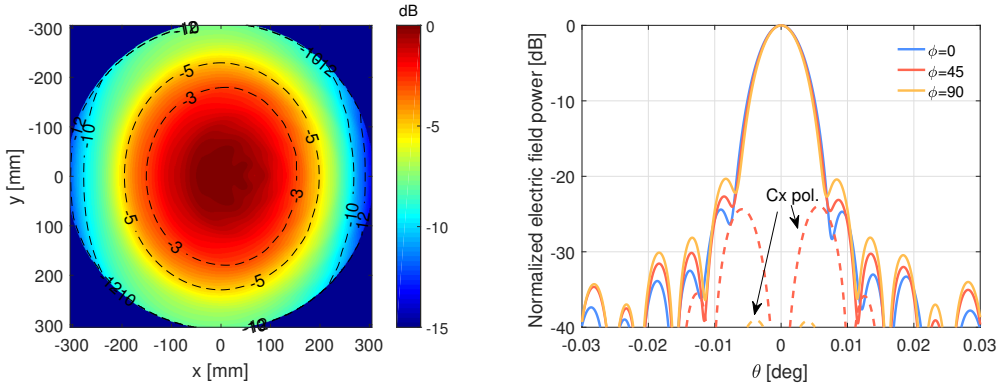

(a) (b)

Fig. 5.2. (a) Illumination of the telescope's secondary mirror and (b) radiation pattern after the telescope's primary mirror for the double-slot lens antenna source of Chapter 2.

50%, respectively. The aperture efficiency is slightly lower due to lower radiation efficiency, as seen in Chapter 2.

The illumination of the telescope's secondary at 350 GHz is shown in Fig. 5.3a for a $2\lambda f_{\#}$ offset pixel in the symmetric plane, where λ is taken at the lowest frequency of the wideband design of Part II. The scanned angle is $\theta = 0.018$ deg and the resulting scan loss is 0.49 dB. The losses associated to a $2\lambda f_{\#}$ pixel in the symmetric plane and in the asymmetric plane are tabulated in Table 5.I. The aperture efficiency of an offset pixel in the symmetric plane is 42%. An offset pixel in the asymmetric plane has 43% aperture efficiency. The small difference is due to a an improved spill-over efficiency in the cold optics for an offset pixel in the asymmetric plane.

5.3 Misalignment tolerance of the optics

A tolerance analysis was performed to quantify the sensitivity of the warm optics to misalignment. The ASTE telescope is fixed and the entire cold or entire warm optics are individually misaligned relative to their designed position. For both the cold and warm optics a translational and rotational misalignment is considered in each of the three axes $\hat{\boldsymbol{x}}, \hat{\boldsymbol{y}}, \hat{\boldsymbol{z}}$ defined in Fig. 5.4. The analysis is done for the central pixel with the field lens, described in Section 4.1, present. The quantities of interest are the variation in Strehl ratio and spill-over loss as a function of the misalignment. These quantities are defined in Appendix B. For perfectly

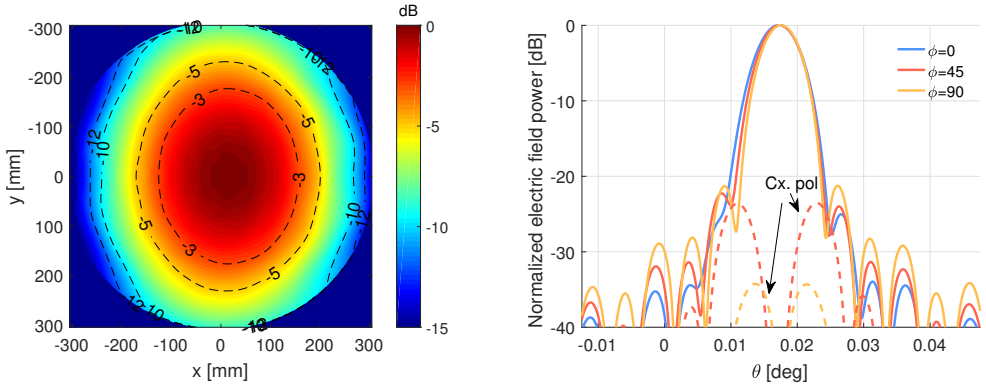

(a) (b)

Fig. 5.3. (a) Illumination of the telescope's secondary mirror and (b) radiation pattern after the telescope's primary mirror for a $2\lambda f_{\#}$ offset double-slot lens antenna source of Chapter 2.

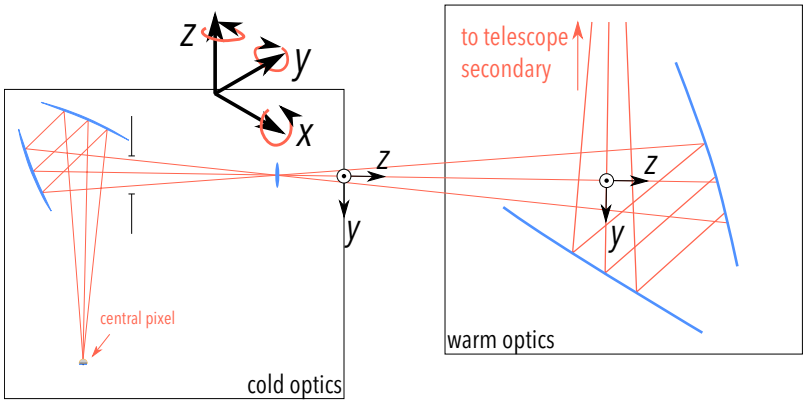

Fig. 5.4. Reference coordinate systems for the tolerance analysis.

aligned optics the achieved Strehl ratio is 1. The additional spill-over loss presented here is relative to the spill-over loss in the perfectly aligned optics.

The additional spill-over loss due to a misalignment is always due to spill over on the telescope's secondary reflector, not due to spill-over in the cold or warm optics. An example is shown in Figs. 5.5a and 5.5b. The reduction in Strehl ratio is due to defocusing, of which an example is shown in Figs. 5.5c and 5.5d.

The results of the tolerance analysis for a misalignment of the cold optics are shown in Fig. 5.6. Rotating the cold optics by $|\theta| \leq 3$ deg still results in a Strehl ratio higher than 0.9 and a spill-over loss lower than 0.1 dB. Rotation around $\hat{\boldsymbol{z}}$ has no influence on the Strehl ratio or spill-over loss. A displacement along $\hat{\boldsymbol{x}}$ or $\hat{\boldsymbol{y}}$ up to 10 mm is allowable to maintain

Table 5.I. Efficiencies and losses after telescope for a 5.2 deg Gaussian beam and the double-slot lens antenna at 350 GHz. FLR stands for field lens reflection.

Efficiency type	Gaussian beam	Double-slot antenna	Offset pixel (symm.)	Offset pixel (asymm.)
$\eta_{\text{radiation}}$ (Chapter 2)	100%	80%	80%	80%
$\eta_{\text{spillover}}$ (Chapters 3 and 4)	94%	73%	67%	69%
η_{FLR} (Chapter 4)	92%	92%	92%	92%
η_{taper}	82%	87%	85%	84%
η_{aperture}	71%	47%	42%	43%
Loss type [dB]	Gaussian beam	Double-slot antenna	Offset pixel (symm.)	Offset pixel (asymm.)
Radiation loss (Chapter 2)	0	0.97	0.97	0.97
Spill-over loss (Chapters 3 and 4)	0.29	1.3	1.71	1.6
FLR loss (Chapter 4)	0.37	0.37	0.37	0.37
Taper efficiency loss	0.88	0.60	0.73	0.74
Aperture efficiency loss	1.54	3.28	3.78	3.68

a Strehl ratio higher than 0.9 and a spill-over lower than 0.5 dB. Shifting along $\hat{\boldsymbol{z}}$ has very little effect on the Strehl ratio or spill-over losses because this is the optical axis.

The results of the tolerance analysis for a misalignment of the warm optics are shown in Fig. 5.7. Rotating the warm optics by $|\theta| \leq 0.5$ deg still results in a Strehl ratio higher than 0.9 and a spill-over loss lower than 0.5 dB. However, the sensitivity to rotations around $\hat{\boldsymbol{z}}$ is much higher than for rotations about $\hat{\boldsymbol{x}}$ or $\hat{\boldsymbol{y}}$. A displacement up to 5 mm along any axis is allowable to maintain a Strehl ratio higher than 0.9 and a spill-over lower than 0.25 dB. For the translation, the sensitivity to displacements along $\hat{\boldsymbol{x}}$ is much higher than for $\hat{\boldsymbol{y}}$ or $\hat{\boldsymbol{z}}$.

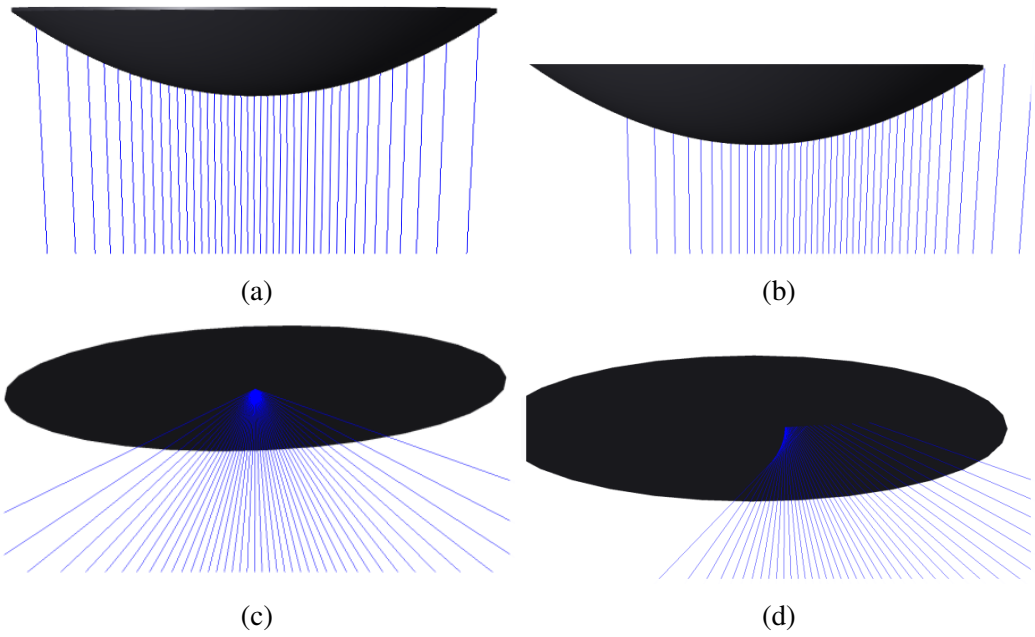

Fig. 5.5. Illustrative effect of misalignment in the optics. (a) and (c) show the baseline spill-over and focusing for well-aligned optics. (b) and (d) show the extra spill-over loss and defocusing due to misaligned optics.

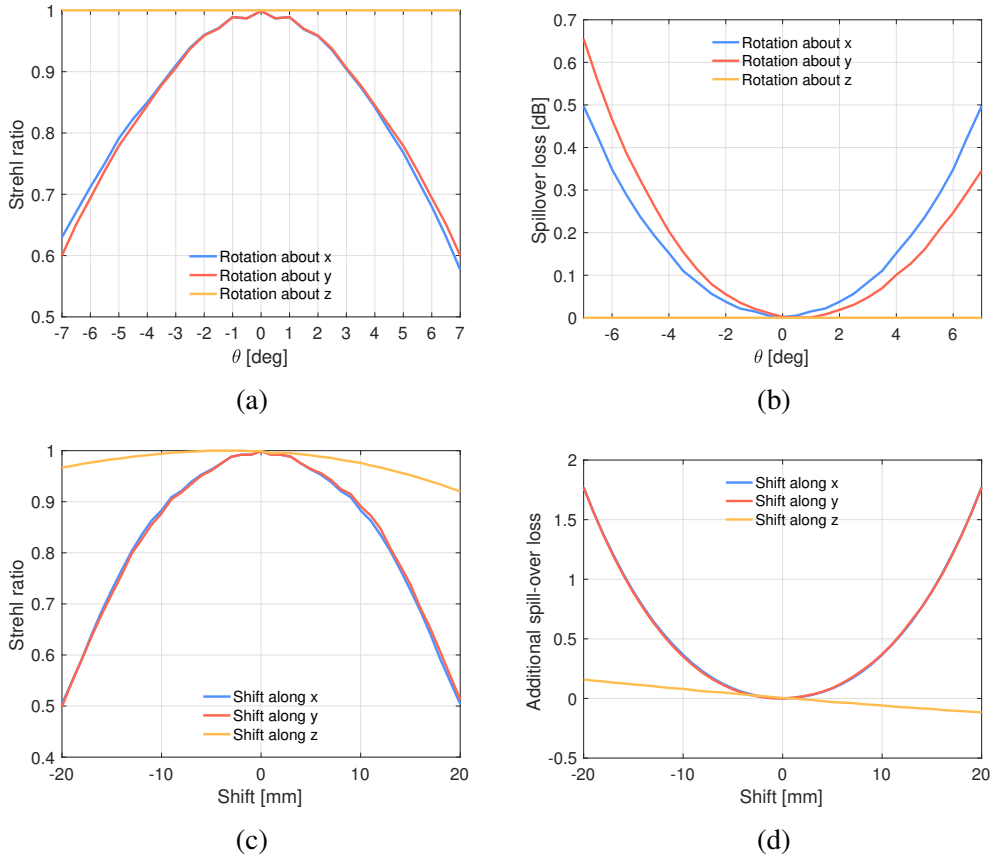

Fig. 5.6. Tolerance of the optics to rotation of the cold optics (a) Strehl ratio and (b) extra spillover losses. Tolerance of the optics to translation of the cold optics (c) Strehl ratio and (d) extra spillover losses.

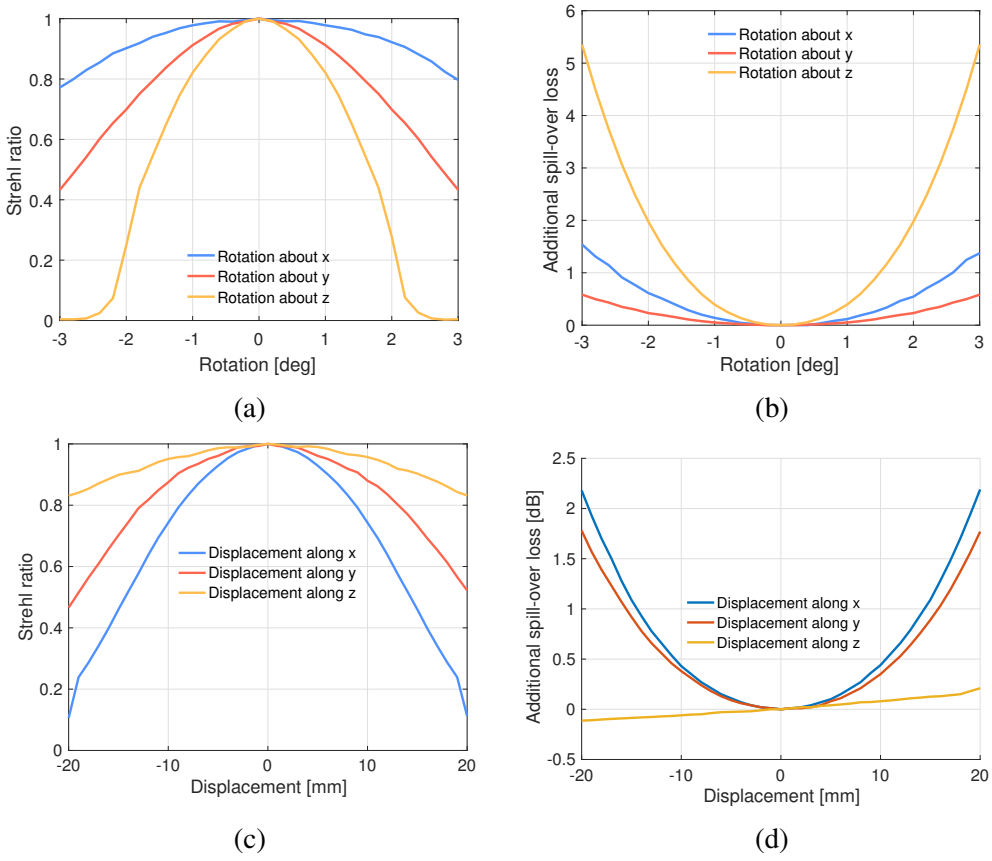

Fig. 5.7. Tolerance of the optics to rotation of the warm optics (a) Strehl ratio and (b) extra spillover losses. Tolerance of the optics to translation of the warm optics (c) Strehl ratio and (d) extra spillover losses.

Chapter 6: Narrowband quasi-optical system conclusion

The performance of the double-slot lens antenna, cold optics, warm optics and complete quasi-optical system has been presented in the frequency range $326 - 368$ GHz for a single-pixel setup. The aperture efficiency of the complete system is 48%, 51% and 50% at $326, 350$ and 368 GHz, respectively, with the variation stemming mainly from the variation of the double-slot lens antenna's radiation efficiency. This performance variation was shown to be caused by the variation in antenna radiation efficiency.

An alternative double-slot elliptical lens design was presented that increases the directivity by 1.2 dB and coupling to the same $\theta_0 = 5.2$ deg Gaussian beam by 12%-points compared to the current design. The improved design uses a differently shaped lens and does not have an anisotropic sapphire wafer. The improved design was not pursued further because the lens geometry was already defined from the beginning.

A field lens was introduced in the cold optics to facilitate multi-pixel operation. Without field lens, the spill-over loss for a $2\lambda f_{\#}$ offset pixel would be 8.5 dB. The introduction of a field lens causes an additional 0.37 dB of field lens reflection losses due to reflections at the air-dielectric interface for all pixels. The scan loss for a $2\lambda f_{\#}$ offset pixel is 0.5 dB.

An extensive tolerance analysis was performed to evaluate the resilience to misalignment. The most sensitive component is the warm optics, which can be rotated up to 0.5 deg to maintain a Strehl ratio higher than 0.9 with an additional spill-over loss lower than 0.5 dB. The warm optics can be displaced up to 5 mm and still maintain a Strehl ratio higher than 0.9 with an additional spill-over loss of 0.25 dB. The sensitivity of the warm optics to misalignment is heavily dependent on the axis of rotation or displacement.

Operation over the complete wideband of $240-720$ GHz is not possible with this antenna since it is narrowband. In Part II a wideband antenna is investigated to meet this requirement.

Part II
Wideband antenna design

In Section 1.2 we have seen that frequency-stable radiation patterns from an antenna at sub-mm wavelengths in a 1:3 frequency bandwidth with the purpose of feeding a high-$f_{\#}$ reflector have not been realized. This challenge is addressed in this Part, in which we present a preliminary investigation into frequency-stable radiation patterns from a single leaky-slot antenna for the DESHIMA spectrometer. A reflector feeder is required that operates over a 1:3 bandwidth with high, constant aperture efficiency for a reflector with $f_{\#} > 2$.

To meet these requirements, we will focus on three design scenarios in Chapter 7:

- In Section 7.1 a straight slot under an elliptical lens is used [9]. The idea is to achieve constant lens illumination surface in terms of wavelength. In principle, the quadratic frequency-dependence of the leaky-slot beams radiated into the lens can then be compensated by using a diffraction-limited elliptical lens (see Appendix E.1).
- In Section 7.2 we taper the leaky slot to improve beam quality and cross-polarization performance [39, p. 114]. Furthermore, this reduces the quadratic frequency dependence of the leaky-slot beams radiated into the lens. We then investigate the performance of this tapered slot under a hyper-hemispherical lens in which the fields are dominated by the geometrical-optics contribution (see Appendix E.2).
- In Section 7.3, using the same tapered leaky slot, we locally taper the airgap at the center of the slot in such a way that only the high-frequencies are affected. The radiated beams inside the lens remain the same at the low frequencies, whereas the beams at high frequencies become wider, which significantly reduces the directivity variation of the primary fields within the entire bandwidth. The performance of this slot under a hyper-hemispherical lens is then investigated.

For all scenarios a parametric study was performed to maximize optical efficiency using Eqs. (B.3) and (B.5).

In Chapter 8 an equivalent, simplified quasi-optical system that models the optics presented in Part I is introduced to quantify the optical efficiency of the quasi-optical system using GRASP for the highest-performing cases that came out of the parametric study.

Finally, in Chapter 9, we provide concluding remarks based on the results that we presented in Chapters 7 and 8. Future work and recommendations are also discussed.

Chapter 7: Leaky lens design

In this Chapter, frequency-stable radiation patterns from the leaky-lens antenna with the goal of constant aperture efficiency on a high-$f_{\#}$ reflector within a 1:3 bandwidth are investigated. In Sections 7.1 to 7.3, the slot geometries of the straight slot, tapered slot and tapered slot with tapered airgap are presented, respectively, along with their primary radiation patterns inside the lens. The silicon lenses that are placed on top of these slots are optimized for optical efficiency in accordance with Eqs. (B.3) and (B.5). This means varying the cut-off angle θ_{co} such that the trade-off between spill-over efficiency and taper efficiency yields the maximum optical efficiency. The secondary patterns after these lenses are evaluated without a matching layer. The reflection efficiency of the lenses are calculated assuming a single $\lambda_{\text{d}}/4$ matching layer at the central frequency, where λ_{d} is the wavelength in the matching layer material. The front-to-back efficiency of the antennas has been calculated as the ratio of power radiated into the dielectric stratification to the total radiated power of the antenna. The radiation efficiency of each lens is stated, but not optimized.

7.1 Straight slot

The straight slot used here is a scaled version of the slot of [9]. The slot width and airgap have been scaled down by a factor 12 to map the frequency band $20-60$ GHz in [9] to $240-720$ GHz used here. The resulting slot is geometrically described by $h = w_s = 42\ \mu\text{m}$. In this region, the leaky-wave angle γ_{lw} is constant and the attenuation constant increases almost linearly with frequency [9, Fig. 6]. The material stratification is shown in Fig. 7.1a and the slot geometry is shown in in Fig. 7.1b. The geometric parameters for the straight slot can be found in Table 7.IV at the end of this Chapter.

The field radiated into the silicon by the straight slot is shown in Fig. 7.2a. We observe the leaky wave angle γ_{lw} is indeed constant at $17\ \text{deg}$ like in [9]. The fields in the $\phi = 90\ \text{deg}$

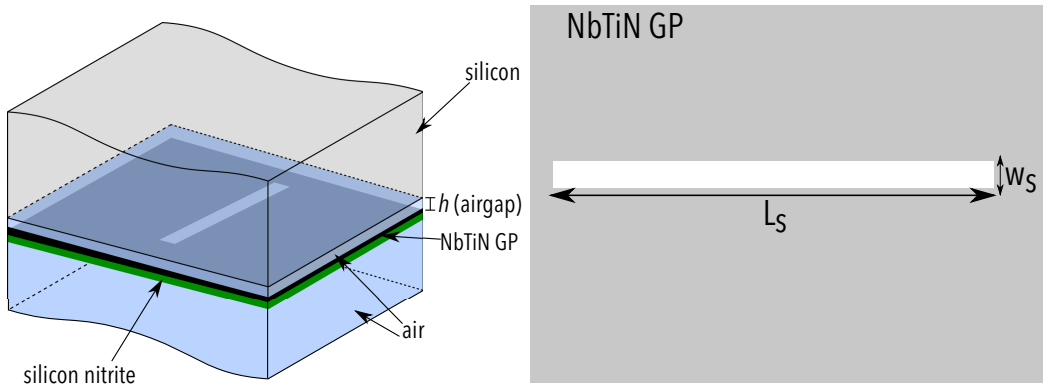

(a) (b)

Fig. 7.1. (a) Semi-infinite material stratification for the straight leaky slot and (b) geometric parameters of the slot.

cut show around 5 dB lower maxima than the fields in the $\phi = 0$ deg cut. The -10 dB point decreases with frequency: from 34 deg at 240 GHz to 23 deg at 720 GHz. The maximum cross-polarization is -2.8 dB at 720 GHz and is observed in the $\phi = 45$ deg cut.

The phase center was determined by minimizing the phase error loss as described in Appendix A. The phase center was taken below the ground plane. The phase error loss as a function of the shift below the ground plane is shown in Fig. 7.2b. We observe the phase center is not constant with frequency. The average phase error loss is lowest, -0.22 dB when the phase center is taken to be 680 μm below the ground plane.

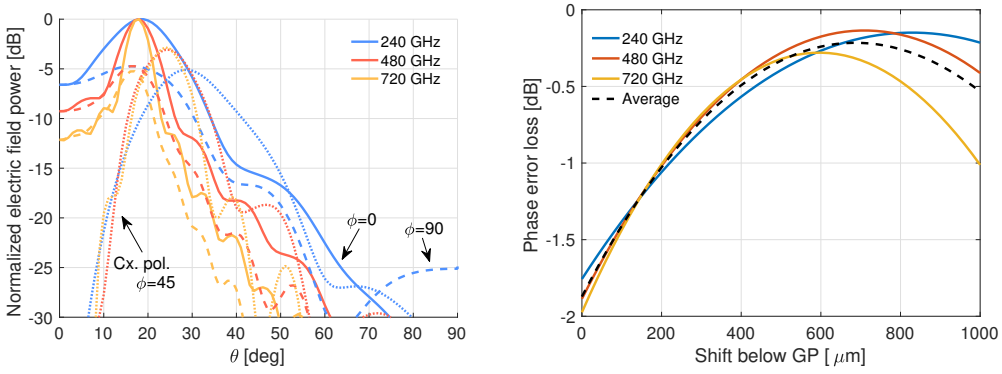

(a) (b)

Fig. 7.2. Normalized fields radiated into the semi-infinite silicon of Fig. 7.1 by (a) the straight slot and (b) the phase error loss as a function of the phase center location below the ground plane.

A silicon synthesized elliptical lens was used in conjunction with the straight slot and optimized for the central frequency. Such an extended hemispherical lens consists of the union of a solid hemisphere of radius R and a cylindrical extension with radius R and height L. The geometry of a synthesized elliptical lens is further explained in Appendix E. The radius of the lens was taken as $R = 3.55$ mm to couple maximally to a Gaussian beam of $\theta_{-11\text{ dB}} = 5.8$ deg (and thus to the existing cold optics) at 480 GHz. Furthermore, this lens radius allows a $2\lambda f_{\#}$ sampling of the focal plane. The lens extension length L was varied from $L = 0.19R$ to $L = 0.39$ to achieve maximum optical efficiency and directivity at this frequency.

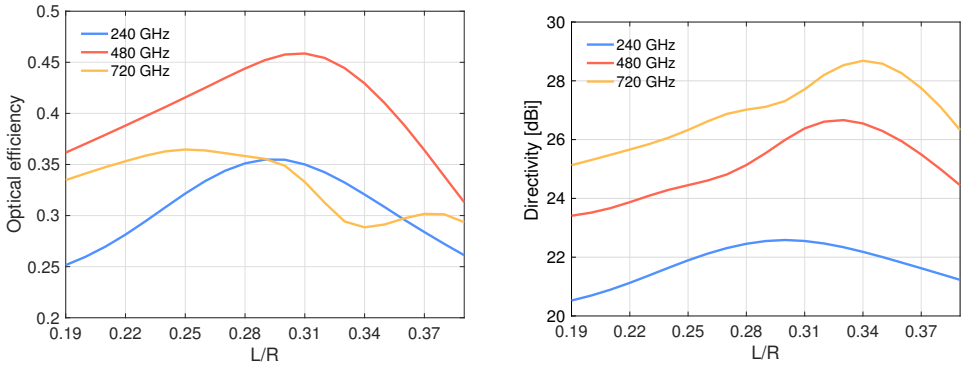

(a) (b)

Fig. 7.3. (a) Optical efficiency and (b) achieved directivity of the straight slot after the silicon lens for $R = 3.55$ mm as a function of the extension length L/R.

The result of this sweep is shown in Fig. 7.3. At 480 GHz, the optical efficiency is maximum, $\eta_{\text{opt}} = 0.46$, at $L/R = 0.31$. A maximum directivity of 26.7 dB is obtained for $L/R = 0.33$ at 480 GHz. The lens with $R = 3.55$ mm and $L/R = 0.33$ was chosen to investigate further. The optical efficiency for this extension length at 480 GHz is $\eta_{\text{opt}} = 0.44$.

The secondary radiation pattern of the straight slot under the synthesized elliptical lens is shown in Fig. 7.4a. The -10 dB beamwidth changes from 11 deg to 5 deg in the 1:3 bandwidth. The cross-polarization is highest at 720 GHz and is observed in the $\phi = 45$ deg plane. The sidelobes are highest, -12 dB, at 240 GHz, which is expected from a leaky-lens antenna without matching layers [47]. At 480 GHz, the main beam matches the $\theta_{-11\text{ dB}}$ Gaussian beam well. The average phase error loss is -0.04 dB when the phase center is taken 12 mm above the ground plane, shown in Fig. 7.4b.

The radiation efficiency of the straight slot under a synthesized elliptical lens using a

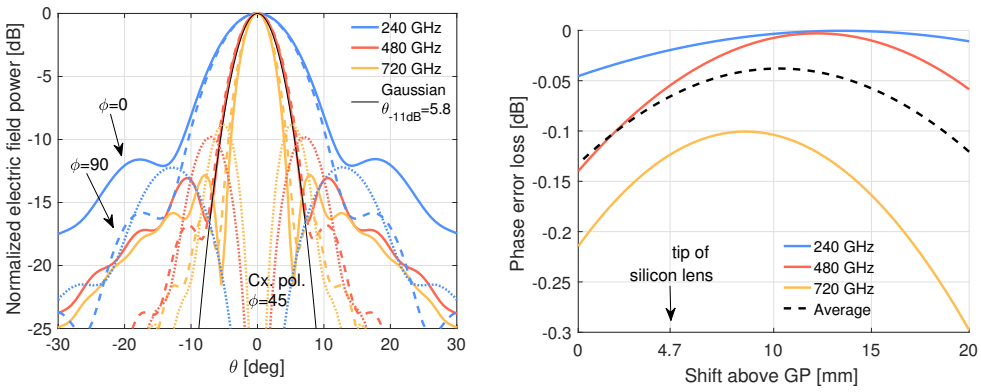

(a) (b)

Fig. 7.4. (a) Secondary radiation pattern and (b) phase error loss of the straight slot under a silicon extended hemispherical lens with $R = 3.55$ mm, $L/R = 0.33$. A Gaussian beam with $\theta_{-11\text{ dB}} = 5.8$ deg is superimposed on the radiation pattern in black.

quarter-wavelength matching layer at 480 GHz is lower than 90% at this frequency. The reflection, front-to-back and radiation efficiencies are given in Table 7.I for all frequencies.

Table 7.I. Reflection, front-to-back and radiation efficiency of the straight slot under a synthesized elliptical lens.

Frequency [GHz]	$\eta_{\text{refl.}}$	$\eta_{\text{F2B.}}$	$\eta_{\text{rad.}}$
240	0.76	0.98	0.74
480	0.98	0.91	0.89
720	0.82	0.83	0.68

7.2 Tapered leaky slot

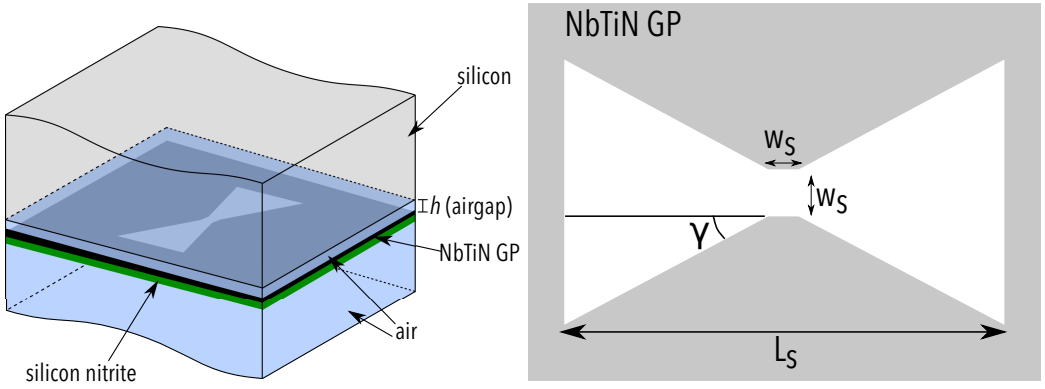

(a) (b)

Fig. 7.5. (a) Semi-infinite material stratification for the tapered leaky slot and (b) geometric parameters of the slot.

The tapered slot used here is a scaled version of the slot described in [39, p. 115]. The material stratification is shown in Fig. 7.5a. The tapering of the slot is done by an angle of $\gamma = 15\ \mathrm{deg}$, which reduces cross-polarization and keeps the power radiated into the broadside direction stable over frequency compared to the straight slot [39]. The slot geometry is shown in Fig. 7.5b. The geometric parameters are listed in Table 7.IV at the end of this Chapter. As a consequence of the tapering, the beams in the primary patterns also widen as seen in Fig. 7.6a. The -10 dB levels are at $50\ \mathrm{deg}$ for 240 GHz and $35\ \mathrm{deg}$ for 720 GHz in the $\phi = 90\ \mathrm{deg}$ cut. The radiation patterns are more symmetric than for the straight slot and the field level at broadside is stable with frequency. The maximum level of cross-polarization is -7.2 dB and is achieved at 720 GHz in the $\phi = 45\ \mathrm{deg}$ cut, which is 5 dB lower than the cross-polarization level of the straight slot.

The phase center is located closer to the center of the slot than the phase center of the straight slot, $320\ \mu\mathrm{m}$ below the ground plane, which results in an average phase error loss of -0.17 dB as shown in Fig. 7.6b.

The lens used with the tapered slot is optimized around a hyper-hemispherical lens, explained in Appendix E.2, leading to a virtual focus below the ground plane. The secondary patterns of the lens are then dominated by the geometric-optics contribution. A parametric analysis as a function of the lens radius R and the normalized extension length L/R was performed to optimize the optical efficiency of the antenna using Eqs. (B.3) and (B.5). The

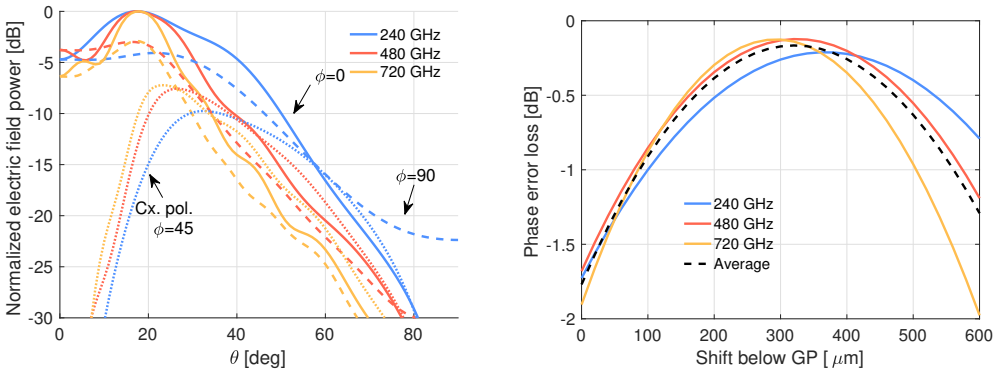

(a) (b)

Fig. 7.6. Normalized fields radiated into the semi-infinite silicon of Fig. 7.5 by (a) the tapered slot and (b) the phase error loss as a function of the phase center location below the ground plane.

smallest lens radius was chosen as 4 mm, which equals the radius of the lens in the narrow-band design of Part I. The largest lens radius was chosen to be 14 mm. The extension length was varied from $L = 0.25R$ to $L = 0.31R$. Since the phase center of the leaky slots is below the ground plane, an extension shorter than $L = 0.29R$ is expected to give geometrically limited radiation.

The results of the parametric study are shown in Fig. 7.7. The minimum calculated optical efficiency over the bandwidth is shown in Fig. 7.7a. The minimum optical efficiency is highest ($\eta_{\text{opt,min}} = 0.61$) when the radius of the lens is 13 mm with a normalized extension length of $L/R = 0.31$. The cut-off angle that maximizes the optical efficiency is shown in Fig. 7.7b and is $\theta_{\text{co}} = 7.3$ deg for the aforementioned lens.

The secondary radiation pattern of the lens with $R = 13$ mm and $L/R = 0.31$ is shown in Fig. 7.8a. The gray area corresponds to the region inside the cut-off angle. The field level at the cut-off angle is -12 dB at all frequencies. Around the broadside angle, there is some variation in frequency caused by the varying lens size in terms of wavelength. The phase error loss as a function of the phase center location below the ground plane is shown in Fig. 7.8b and the phase center is taken 74 mm below the ground plane. It should be noted that the phase center is not unique over the 1:3 bandwidth.

While the design above is maximized with regards to optical efficiency, it does not allow $2\lambda f_{\#}$ sampling of the focal plane (see overlay of Fig. 7.7a). Therefore, a second design with $R = 7, L = 0.31$ was evaluated. The highest minimum optical efficiency of this lens is $\eta_{\text{opt,min}} = 0.53$. The cut-off angle θ_{co} of this second design is close to the design angle of the

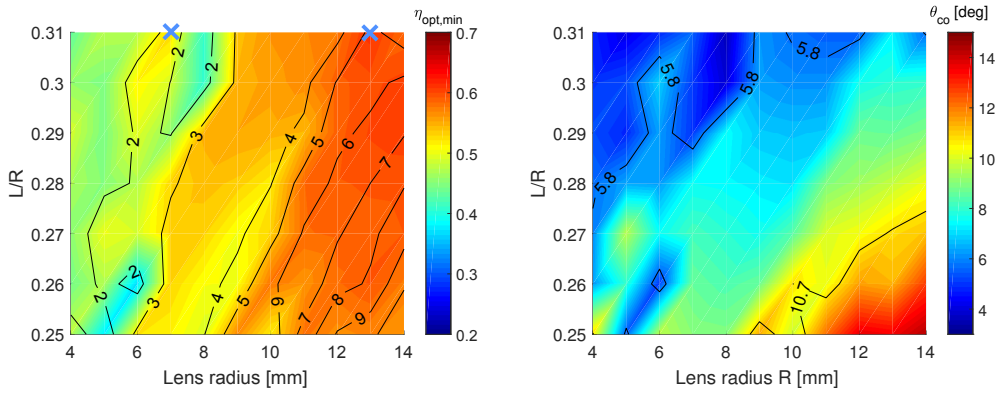

(a) (b)

Fig. 7.7. (a) Minimum (in frequency) achieved optical efficiency and (b) corresponding cut-off angle θ_{co} that maximizes it of the tapered slot under the hyperhemispheric lens as a function of R and L/R in the frequency band of $240 - 720$ GHz. Superimposed on (a) is the lens diameter $D = 2R$ in terms of $\lambda f_{\#}$ in free-space at 240 GHz. In (b) the geometrically expected -11 dB angle for a hyper-hemispheric lens and the -11 dB design angle of the cold optics are overlaid.

current cold optics of Part I. Therefore, this design can be used to achieve $2\lambda f_{\#}$ sampling of the focal plane using the current cold optics at the cost of lower optical efficiency than the previously described lens. The secondary radiation pattern from this lens is shown in Fig. 7.9a. The phase center is taken 49 mm below the ground plane, but, as becomes clear from Fig. 7.9b, the phase center location presents a trade-off in phase efficiency between different frequencies.

The reflection efficiency of both cases for the tapered slot under an extended hemispherical lens using a quarter-wavelength matching layer at 480 GHz is the same, since the normalized extension length, $L/R = 0.31$, is the same in both cases. Furthermore, the front-to-back efficiency is determined by the slot, not by the lens, meaning η_{F2B} is the same for both lenses, too. The radiation efficiency is 93% at the central frequency. The reflection, front-to-back and radiation efficiencies are given in Table 7.II for all frequencies.

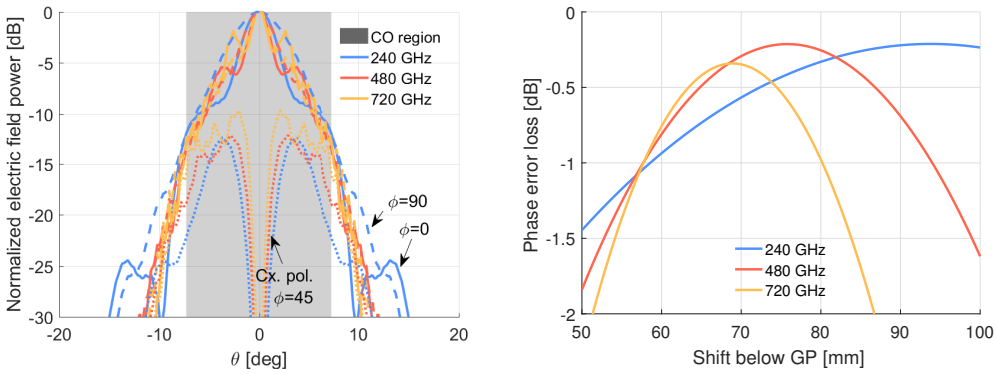

(a) (b)

Fig. 7.8. Maximum optical efficiency scenario: (a) Secondary radiation pattern and (b) phase error loss of the tapered slot under a silicon extended hemispherical lens with $R = 13$ mm, $L/R = 0.31$.

Table 7.II. Reflection, front-to-back and radiation efficiency of the tapered slot under an extended hemispherical lens with $L/R = 0.31$.

Frequency [GHz]	$\eta_{\text{refl.}}$	$\eta_{\text{F2B.}}$	$\eta_{\text{rad.}}$
240	0.77	0.99	0.76
480	0.98	0.94	0.93
720	0.83	0.89	0.74

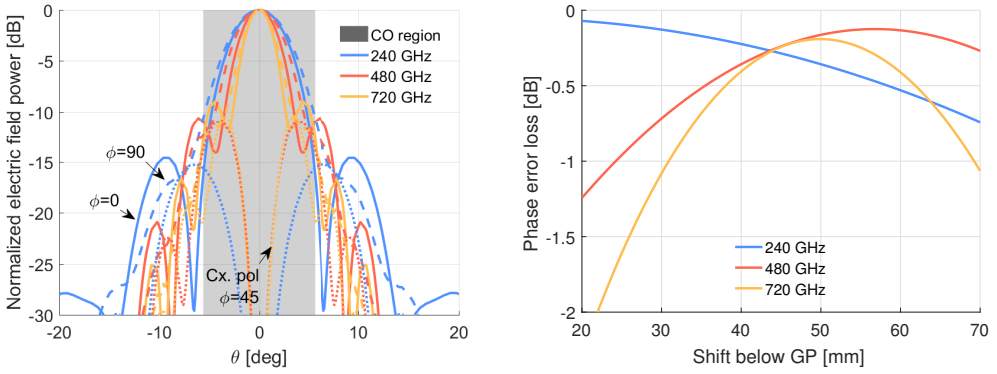

(a) (b)

Fig. 7.9. $2\lambda f_{\#}$ sampling scenario: (a) Secondary radiation pattern and (b) phase error loss of the tapered slot under a silicon extended hemispherical lens with $R = 7$ mm, $L/R = 0.31$.

7.3 Tapered leaky slot with tapered airgap

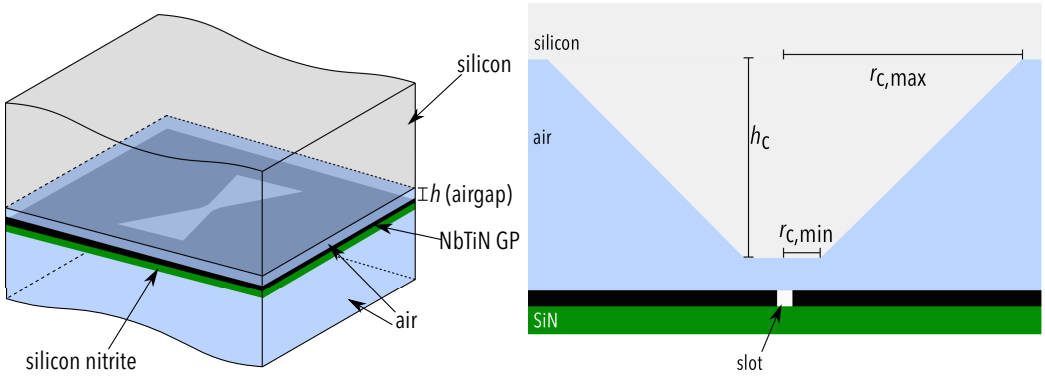

Fig. 7.10. (a) Semi-infinite material stratification for the tapered leaky slot with a tapered airgap and (b) geometric parameters describing the conic tapering of the airgap.

The tapered leaky slot with tapered airgap is a new slot concept with the aim of stabilizing the primary radiation patterns with frequency. The idea is to create an airgap that is small near the center of the slot and then increases with the radial distance from the center of the slot, shown in Fig. 7.10b. If the attenuation constant is frequency-dependent, different frequencies will experience a varying absolute airgap but this airgap is constant in terms of wavelength. This tapering is combined with the slot tapering of Section 7.2 to keep the radiation levels at broadside constant and reduce cross-polarization levels.

The slot geometry is the same as the tapered slot shown before in Section 7.2. The parameters of the tapered airgap were chosen as follows. The cone's minimum radius $r_{c,\text{min}}$ was chosen to be large with respect to the slot width w_s. Its maximum radius $r_{c,\text{max}}$ was chosen such that the current along the slot has attenuated by 10 dB at 720 GHz but introduces negligible effect on the current of the lowest frequency of 240 GHz. The height of the cone h_c was chosen such that the smallest airgap is in the order of $\lambda/100$ at the highest frequency. Some optimization of these parameters was then performed to obtain maximum frequency stability in the primary radiation patterns. The final geometric parameters are given in Table 7.IV at the end of this Chapter.

The primary radiation patterns are shown in Fig. 7.11a. The patterns are very stable with frequency and show good symmetry. The -15 dB level is 60 deg for all frequencies. The maximum cross-polarization is approximately -10 dB at all frequencies, which is up to 3 dB

lower than the tapered slot with constant airgap. The fields are also more uniform along the broadside with a variation less than 2 dB. The phase error loss is shown in Fig. 7.11b and is minimum, -0.08 dB, when the phase center is taken 380 μm below the ground plane.

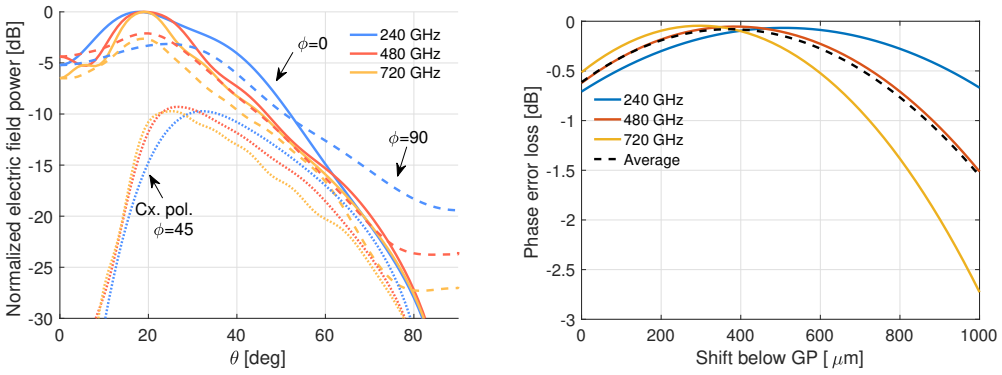

(a) (b)

Fig. 7.11. Normalized fields radiated into the semi-infinite silicon of Fig. 7.10 by (a) the tapered slot and (b) the phase error loss as a function of the phase center location below the ground plane.

For this slot we also perform a parametric analysis over the lens radii $R = 4$ mm to $R = 14$ mm and the normalized lens extension lengths $L/R = 0.25$ to $L/R = 0.31$. This is the same range as in Section 7.2 to study the impact of the new leaky slot concept. For each lens size we find the secondary pattern and the optical efficiency using Eqs. (B.3) and (B.5). The same two scenarios as in Section 7.2 are investigated: the one that provides the highest and most stable optical efficiency and a case in which $2\lambda f_{\#}$ sampling is possible using the cold optics described in Part I. The results are shown in Fig. 7.12. The minimum optical efficiency is reported in Fig. 7.12a and the corresponding cut-off angle θ_{co} is shown in Fig. 7.12b.

The lens with the highest, most stable optical efficiency is found as $R = 14$ mm, $L/R = 0.31$ with $\eta_{\text{opt,min}} = 0.63$. This optical efficiency is achieved when $\theta_{\text{co}} = 7.7$ deg. The secondary radiation pattern of this lens is shown in Fig. 7.13a. At the low frequencies, the field level at θ_{co} is -11 dB. At the highest frequency, the level at θ_{co} is around -7 dB but the field decays more quickly at angles $\theta > \theta_{\text{co}}$ compared to the lowest frequency. The maximum cross-polarization is -11 dB and is observed in the $\phi = 45$ deg cut. The phase error loss over the 1:3 band as a function of shift below the ground plane is shown in Fig. 7.13b. There is a large variation in the position that minimizes the phase error loss. For the evaluation the phase center was taken at 74 mm below the ground plane.

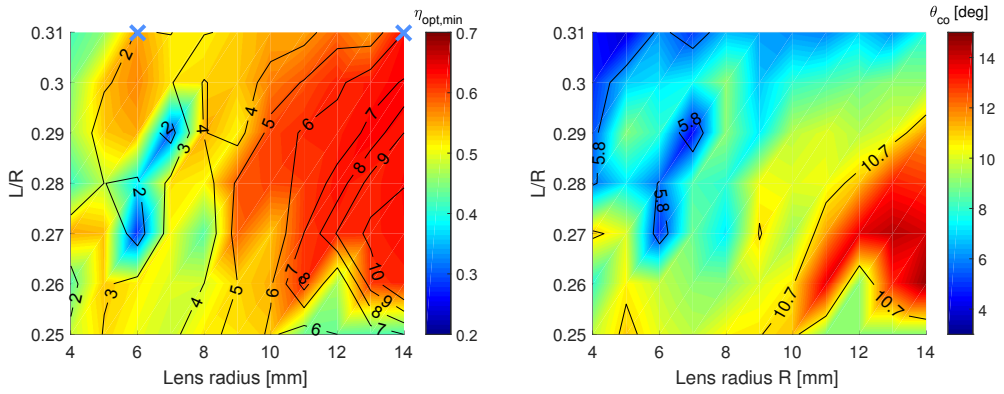

(a) (b)

Fig. 7.12. (a) Minimum (in frequency) achieved optical efficiency and (b) corresponding -11 dB angle that maximizes it of the tapered slot with tapered airgap under an extended hemispheric lens as a function of R and L/R in the frequency band of $240 - 720$ GHz. Superimposed on (a) is the lens diameter $D = 2R$ in terms of $\lambda f_{\#}$ in free-space at 240 GHz. In (b) the geometrically expected -11 dB angle for a hyper-hemispheric lens and the -11 dB design angle of the cold optics are overlaid.

The lens with $R = 6$ mm, $L/R = 0.31$ has the highest $\eta_{\text{opt,min}} = 0.56$ while still permitting $2\lambda f_{\#}$ sampling of the focal plane. The radiation pattern of this lens antenna is shown in Fig. 7.14a. There is a significant variation in beamwidth with frequency. The phase efficiency is again a trade-off between the frequencies, as can be seen in Fig. 7.14b.

As we have seen in the previous Section, the radiation efficiency of the two selected leaky-lens designs are equal because they have the same normalized extension length and use the same tapered slot with tapered airgap. Compared to the tapered slot, the front-to-back efficiency is higher over the whole 1:3 bandwidth. The reflection efficiency is comparable to the tapered slot. The radiation efficiency is 95% at the central frequency. The reflection, front-to-back and radiation efficiencies are given in Table 7.III for all frequencies.

Table 7.III. Reflection, front-to-back and radiation efficiency of the tapered slot with tapered airgap under an extended hemispherical lens with $L/R = 0.31$.

Frequency [GHz]	$\eta_{\text{refl.}}$	$\eta_{\text{F2B.}}$	$\eta_{\text{rad.}}$
240	0.77	0.99	0.76
480	0.97	0.98	0.95
720	0.82	0.96	0.79

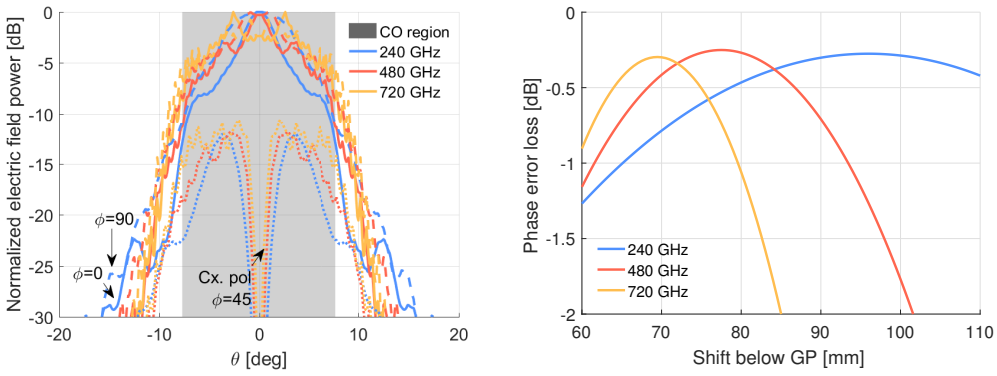

(a) (b)

Fig. 7.13. Maximum optical efficiency scenario: (a) Secondary radiation pattern and (b) phase error loss of the tapered slot with tapered airgap under a silicon extended hemispherical lens with $R = 14$ mm, $L/R = 0.31$.

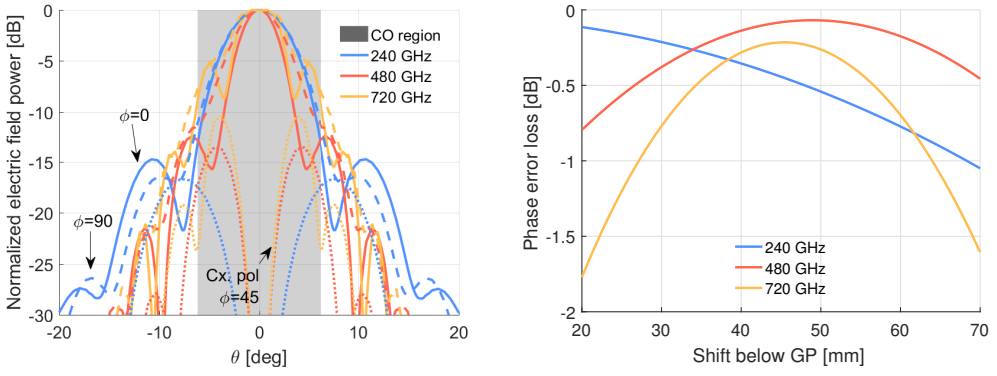

(a) (b)

Fig. 7.14. $2\lambda f_{\#}$ sampling scenario: (a) Secondary radiation pattern and (b) phase error loss of the tapered slot with tapered airgap under a silicon extended hemispherical lens with $R = 6$ mm, $L/R = 0.31$.

Table 7.IV. Geometric parameters of the straight slot,tapered slot and the tapered slot with tapered airgap.

	Straight slot	Tapered slot	Tapered slot with tapered airgap
Slot length (L_s)	2500 μm	2500 μm	1500 μm
Airgap (h)	42 μm	17.5 μm	17.5 μm
Slot width (w_s)	42 μm	3 μm	3 μm
Taper angle (γ)	0 deg	15 deg	15 deg
SiN thickness	1 μm	1 μm	1 μm
Cone height (h_c)	N/A	N/A	15 μm
Cone max. radius ($r_{c,\text{max}}$)	N/A	N/A	200 μm
Cone min. radius ($r_{c,\text{min}}$)	N/A	N/A	30 μm

Chapter 8: Performance of the leaky-lens antennas in an equivalent quasi-optical system

This Chapter discusses an equivalent quasi-optical system for the evaluation of the leaky-lens antennas selected in Chapter 7. The goal of this system is to be optically equivalent to the central pixel of the quasi-optical system of DESHIMA-on-ASTE, but have a variable input $f_{\#}$ to match the leaky-lens antenna designs. Furthermore, an indication of the leaky-lens antennas' performance on the telescope can be evaluated without resorting to a complete redesign of the optics. In Section 8.1, the geometry of the equivalent optics is described. In Section 8.2, the quasi-optical system aperture efficiencies of the selected leaky-lens antennas are given. At the end of this Chapter, Table 8.I gives an overview of the performance of each lens.

8.1 Geometrical description and verification

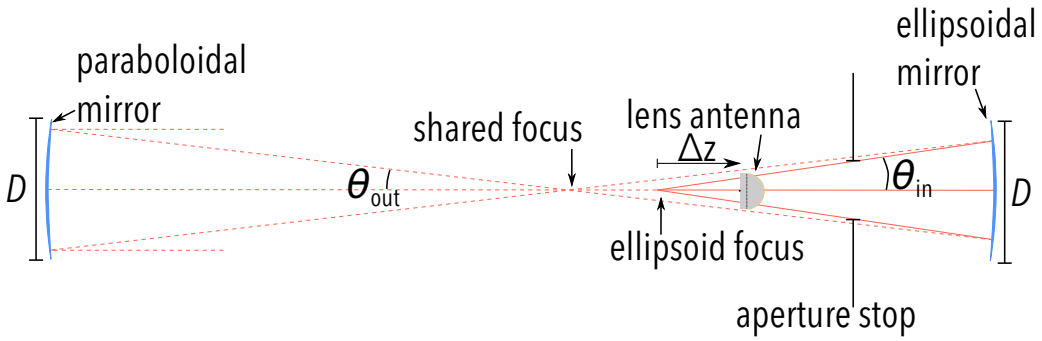

Fig. 8.1. Equivalent optical layout (not to scale).

As we have seen in Part I, the quasi-optics of DESHIMA consist of cold optics, warm optics and the ASTE telescope. In the equivalent optics, the cold optics are modeled only by

an aperture stop. Since the cold optics have unity magnification, this is a reasonable model. The warm optics are modeled by a single symmetric ellipsoidal mirror which matches the $f_{\#}^{\text{ant}}$ of the antenna to the $f_{\#}^{\text{tel}}$ of the telescope. The $f_{\$}^{\text{ant}}$ is calculated as $f_{\$}^{\text{ant}} = 1/2 \tan\theta_{\text{co}}$, where θ_{co} is the geometrical-optics cut-off angle from the antenna to the paraboloid such that the optical efficiency is maximized. For a Gaussian beam, the cut-off angle θ_{co} is equal to its -11 dB angle and the resulting optical efficiency is 82% [22]. The telescope is modeled with a symmetric paraboloidal mirror that has an $f_{\#}^{\text{tel}} = 9.2$ equal to that of the ASTE telescope secondary. The phase center of the antenna under investigation is placed in the first focus of the ellipsoid. This requires the ground plane of the antenna to be shifted a distance Δz towards the ellipsoid, as we have seen in Chapter 7. The aperture is placed between these two components. Finally, the focus of the paraboloid is placed in the second focus of the ellipsoid. The equivalent optics are shown schematically in Fig. 8.1.

The dimensions of the equivalent optics were chosen as follows. The diameter of the aperture was taken as 40 mm. The distance from the ellipsoid focus to the aperture is chosen such that the field level is -15 dB at the edge of the aperture for the specific antenna under investigation. The aperture diameter and field level at its edge are then equal to the design in Part I. The diameters of the ellipsoid and paraboloid are fixed at $D = 300$ mm, which is approximately the size of the reflectors in the warm optics. The input focal length of the ellipse is calculated as $F_{\text{in}} = D/4 \tan\theta_{co}$ which is selected such that the ellipsoid is always over-dimensioned compared to the input beam. The focal length of the paraboloid is fixed at 2.8 m to match the $f_{\#}^{\text{tel}}$ of the telescope secondary. Assuming a Gaussian beam input at the ellipsoid focus of Fig. 8.1, the geometrical-optics edge taper of the paraboloid is then -11 dB and the spill-over loss on the ellipsoid is very low, as seen in Part I.

To verify the optical model, a Gaussian beam with $\theta_{\text{co}} = \theta_{-11\text{ dB}} = 5.8$ deg and $\Delta z = 0$ was used as source. The result of this simulation is shown in Fig. 8.2.

The radiation pattern after the telescope, shown in Fig. 8.2a, gives results consistent with a constant-taper illumination of the parabola. The radiation pattern narrows as the frequency increases, yet the side-lobes stay constant at-24 dB. As expected for a Gaussian source in an optical system with only symmetric reflectors, there is no cross-polarization. In Fig. 8.2b we see the spill-over and taper efficiency are nearly constant over the entire frequency range and always higher than 90%. This leads to an optical efficiency of 82% over the entire frequency range, which is consistent with the Gaussian beam theory in [22].

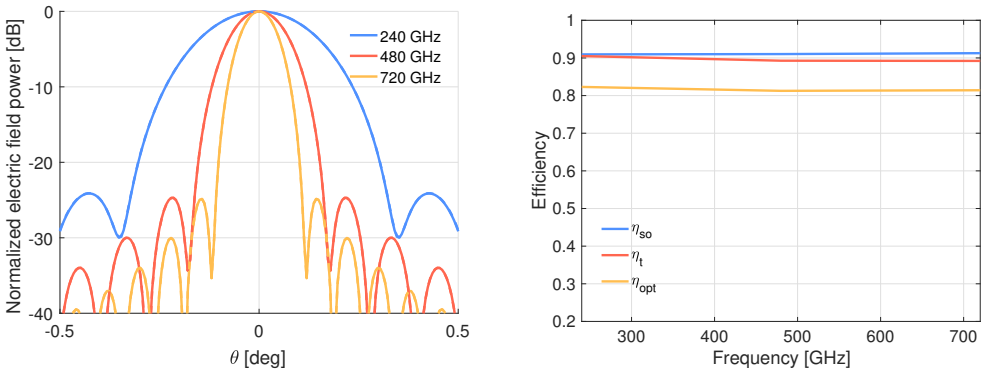

(a) (b)

Fig. 8.2. Gaussian source as input to the equivalent optics. (a) Radiation pattern after the parabola and (b) spill-over, taper and optical efficiency of the Gaussian source.

8.2 Leaky-lens antenna performance

After verification of the optical system with a Gaussian source, the antennas from Chapter 7 are evaluated in the optical system.

8.2.1 Straight leaky slot

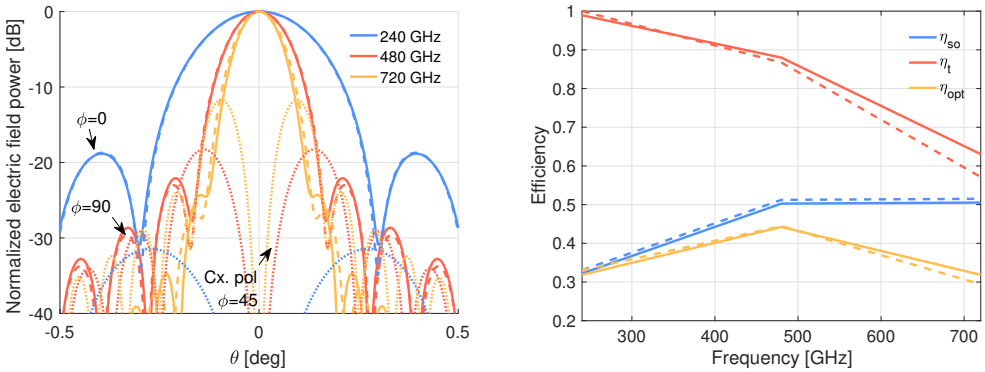

(a) (b)

Fig. 8.3. Straight leaky slot under a synthesized elliptical lens as input to the equivalent optics. (a) Radiation pattern after the parabola and (b) spill-over, taper and optical efficiency of the antenna. The dashed lines in (b) represent the calculations of Chapter 7, the solid lines are calculated using the equivalent optics described in this Chapter.

The optimized straight leaky slot under a synthesized elliptical lens of Section 7.1 ($R = 3.55\ \mathrm{mm}, L/R = 0.33$) was used as a source in the equivalent optical model. From the radiation patters after the parabola in Fig. 8.3a, we see the side-lobes become lower with frequency. This indicates the illumination of the parabola is not constant with frequency. The maximum cross-polarization level increases with frequency, which is consistent with the secondary radiation pattern of the antenna seen in Fig. 7.4a.

The expected optical efficiency is $\eta_{\text{opt}} = 0.44$ at $480\ \mathrm{GHz}$. In Fig. 8.3b, the results of the equivalent optics model are shown along with the results obtained in Chapter 7. We see that the calculated values using the approach of Chapter 7 closely match the values obtained in the equivalent optics. At the central frequency of $480\ \mathrm{GHz}$, the optical efficiency that the lens extension was optimized for matches very well: $\eta_{\text{opt}} = 0.44$.

Compared to the Gaussian beam input in Fig. 8.2, the spill-over efficiency at the design frequency ($480\ \mathrm{GHz}$) is very low, caused by high sidelobes in the secondary radiation pattern of this leaky lens and high cross-polarization, both observed in Fig. 7.4a. It has been demonstrated in [47] that the inclusion of multiple matching layers can significantly decrease the side-lobe level, thereby increasing spill-over efficiency. The taper efficiency at the design frequency is almost 90%, which is a good match to the theoretical optimum.

At the lowest frequency, the radiation pattern of the leaky lens is too wide, causing low spill-over efficiency and high taper efficiency. At the highest frequency, the opposite is observed: high spill-over efficiency but low taper efficiency due to the beam at $720\ \mathrm{GHz}$ being too narrow. Both the low and high frequencies therefore have very low optical efficiencies: $\eta_{\text{opt}} \approx 0.32$.

It is clear from Fig. 8.3 that there is a large frequency dispersion of this leaky lens in terms of optical efficiency.

8.2.2 Tapered leaky slot

The two tapered slot designs of Section 7.2 were then used as a feed in the equivalent optical model. The radiation pattern after the parabola for the optimal design in terms of optical efficiency ($R = 13, L/R = 0.31$) is shown in Fig. 8.4a. At all frequencies, the beams are not well-focused and show high sidelobes in the $\phi = 0$-cut. The cross-polarization increases with frequency, as expected from the antenna radiation pattern.

The resulting efficiencies for the optimal design in terms of optical efficiency are shown

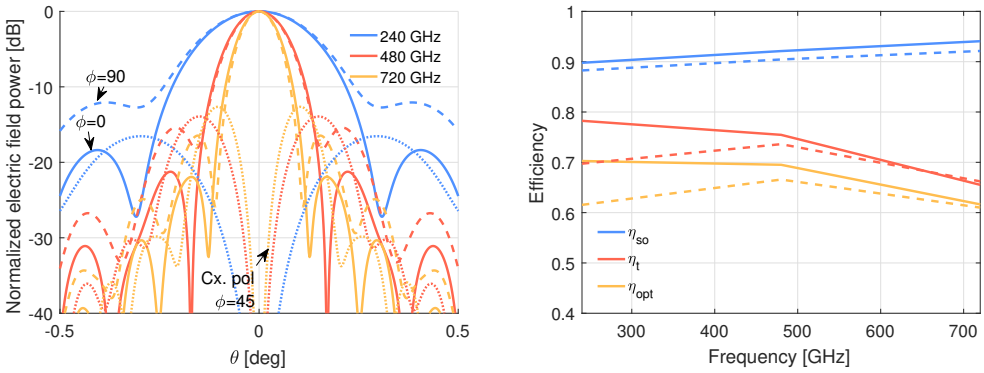

(a) (b)

Fig. 8.4. Optimal η_{opt} design of the tapered leaky slot under an extended hemispherical lens as input to the equivalent optics. (a) Radiation pattern after the parabola and (b) spill-over, taper and optical efficiency of the antenna. The dashed lines in (b) represent the calculations of Chapter 7, the solid lines are calculated using the equivalent optics described in this Chapter.

in Fig. 8.4b. Compared to the straight leaky slot design, the optical efficiency is much higher and more stable, peaking at 0.7% at 240 GHz and decreasing to 63% at 720 GHz. The reason for this decrease is the taper efficiency, which decreases with frequency due to side-lobes in the $\phi = 0$-cut and the increased cross-polarization level of the antenna pattern.

The radiation pattern after the parabola for the $2\lambda f_{\#}$ design ($R = 7, L = 0.31$) is shown in Fig. 8.5a. Again, the beams are not well-focused and show high sidelobes in the $\phi = 0$-cut. The cross-polarization increases with frequency, as expected from the antenna radiation pattern.

The resulting efficiencies for the $2\lambda f_{\#}$ design are shown in Fig. 8.5b. Compared to the straight leaky slot design, the optical efficiency of this lens is higher and more stable, being $\eta_{\text{opt}} > 0.54$ over the whole band. The spill-over and taper efficiency are quite stable but both peak at the central frequency, which causes the optical efficiency to peak there too.

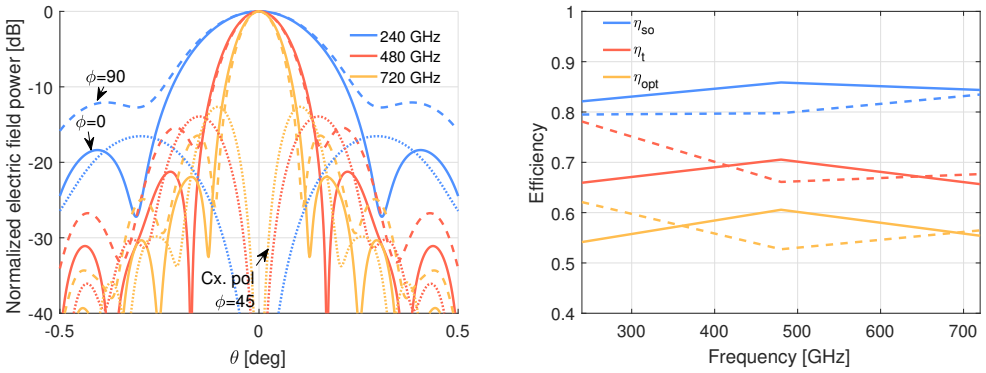

(a) (b)

Fig. 8.5. $2\lambda f_{\#}$ design of the tapered leaky slot under an extended hemispherical lens as input to the equivalent optics. (a) Radiation pattern after the parabola and (b) spill-over, taper and optical efficiency of the antenna. The dashed lines in (b) represent the calculations of Chapter 7, the solid lines are calculated using the equivalent optics described in this Chapter.

8.2.3 Tapered leaky slot with tapered airgap

Finally, the two tapered slot designs with tapered airgap of Section 7.3 were used as a feed in the equivalent optical model. For the optimal design in terms of of optical efficiency ($R = 14, L/R = 0.31$), the radiation patterns after the telescope are shown in Fig. 8.6a. As we have seen in the tapered slot design, here too the beams are not well-focused and show high sidelobes in the $\phi = 0$-cut. The cross-polarization has a maximum of -16 dB in the $\phi = 45$ deg-cut at 480 GHz and is lower at the other frequencies. This is lower than the cross-polarization level of the tapered slot, due to the decreased cross-polarization in the primary pattern of the tapered slot with tapered airgap compared to the regular tapered slot.

The resulting efficiencies for the optimal design in terms of optical efficiency are shown in Fig. 8.6b. The spill-over efficiency is very constant and near the maximum theoretical for a Gaussian beam that we have seen in Fig. 8.2b. Compared to the tapered leaky slot design, the taper efficiency is higher, especially at 480 and 720 GHz. The resulting optical efficiency is higher than $\eta_{\text{opt}} = 0.69$ over the 1:3 bandwidth.

For the $2\lambda f_{\#}$ design ($R = 6, L/R = 0.31$), the radiation patterns after the telescope are shown in Fig. 8.7a. The beams at all frequencies in the $\phi = 90$-cut are not well-focused and wider than their counterparts in the $\phi = 0$-cut. The sidelobe level is lower than -21 dB in the $\phi = 0$-cut. Compared to the $2\lambda f_{\#}$ design with the tapered slot, the maximum cross-

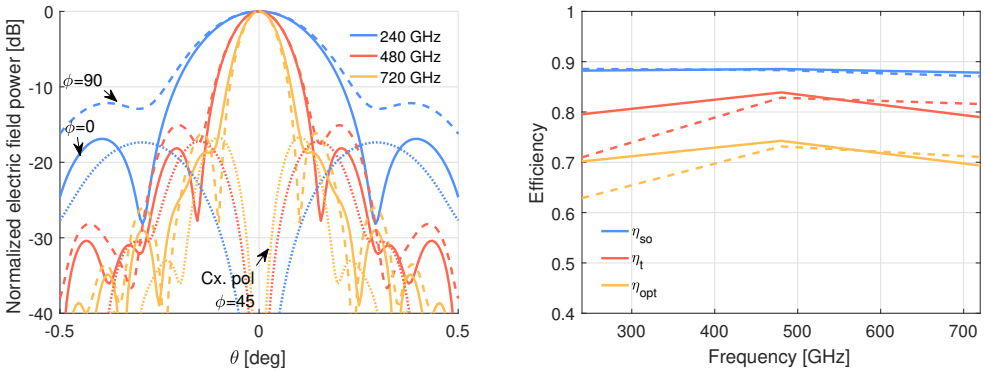

(a) (b)

Fig. 8.6. Optimal η_{opt} design of the tapered leaky slot with tapered airgap under an extended hemispherical lens as input to the equivalent optics. (a) Radiation pattern after the parabola and (b) spill-over, taper and optical efficiency of the antenna. The dashed lines in (b) represent the calculations of Chapter 7, the solid lines are calculated using the equivalent optics described in this Chapter.

polarization level is 5 dB lower at 720 GHz and 4 dB lower at 240 GHz. This is due to the inherently lower cross-polarization of the tapered leaky slot with tapered airgap compared to the regular tapered slot.

The resulting efficiencies for the optimal design in terms of optical efficiency are shown in Fig. 8.7b. The spill-over efficiency is higher than 80% from $240-480$ GHz and drops to 77% at 720 GHz. The taper efficiency increases monotonously with frequency. Compared to the tapered leaky slot design with $2\lambda f_{\#}$, the taper efficiency is higher at 720 GHz, $\eta_t = 0.81$. The resulting optical efficiency is between $\eta_{\text{opt}} = 0.54$ at 240 GHz and $\eta_{\text{opt}} = 0.64$ at 720 GHz.

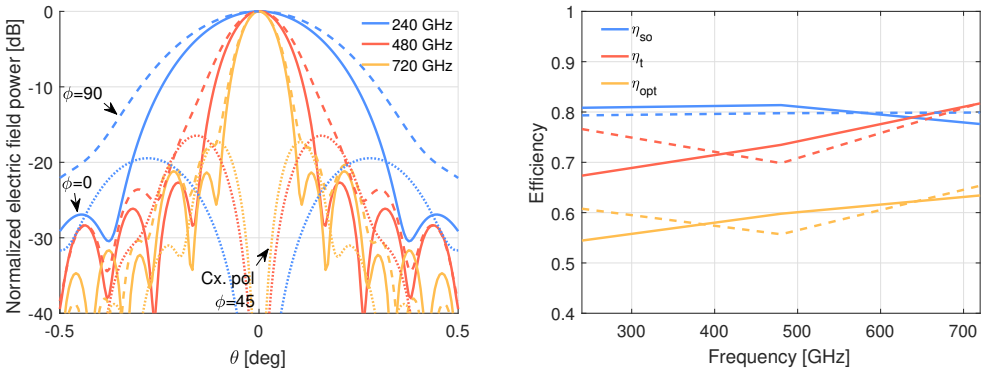

(a) (b)

Fig. 8.7. $2\lambda f_{\#}$ design of the tapered leaky slot with tapered airgap under an extended hemispherical lens as input to the equivalent optics. (a) Radiation pattern after the parabola and (b) spill-over, taper and optical efficiency of the antenna. The dashed lines in (b) represent the calculations of Chapter 7, the solid lines are calculated using the equivalent optics described in this Chapter.

8.2.4 Comparison of radiation patterns and efficiencies

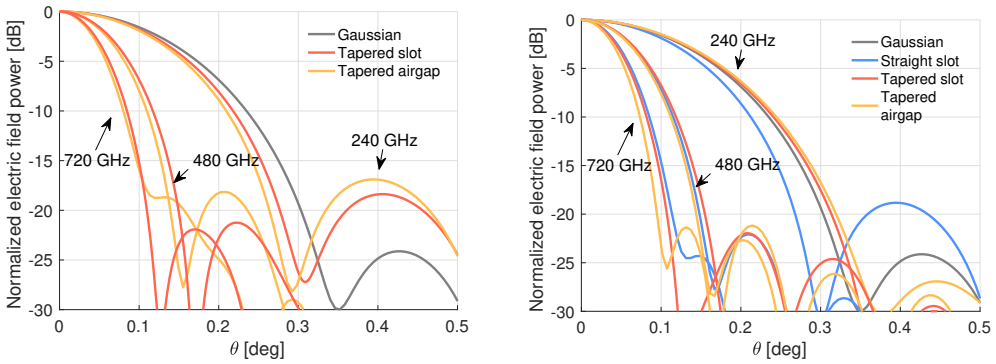

(a) (b)

Fig. 8.8. Comparison of radiation patterns in the $\phi = 0$-cut after the telescope. (a) The discussed cases optimized for η_{opt} and (b) the discussed cases that allow $2\lambda f_{\#}$ spacing.

A comparison of the radiation patterns obtained in the $\phi = 0$-cut in the 1:3 bandwidth is shown in Figs. 8.8a and 8.8b for the cases optimizing the optical efficiency and the $2\lambda f_{\#}$ cases, respectively. The variation in beamwidth and sidelobe level is apparent.

A comparison of the optical and aperture efficiencies in the 1:3 bandwidth is shown in Figs. 8.9a and 8.9b for the cases optimizing the optical efficiency and the $2\lambda f_{\#}$ cases, re-

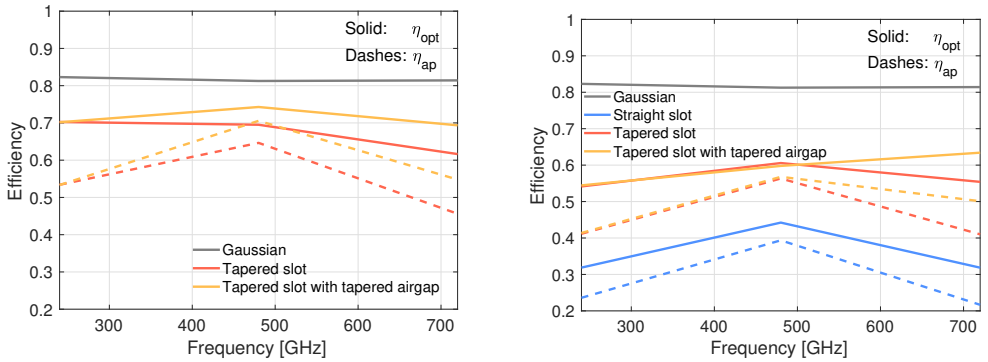

(a) (b)

Fig. 8.9. Comparison of achieved optical and aperture efficiencies of (a) the discussed cases optimized for η_{opt} and (b) the discussed cases that allow $2\lambda f_{\#}$ spacing.

spectively. The aperture efficiencies is the multiplication of the optical efficiency with the radiation efficiency of each slot.

Table 8.I. Summary of performance of the selected leaky-lens antennas of Chapter 7 in the equivalent quasi-optical system presented in this Chapter. The straight, tapered and tapered airgap slot types refer to the geometries described in Sections 7.1 to 7.3, respectively.

Slot type	R [mm]	L/R	Optimized for	$f_{\#}^{\text{ant}}$	$\eta_{\text{opt,min}}$	$\eta_{\text{opt,max}}$	Performance limitation in the quasi-optical system
Straight	3.55	0.33	$2\lambda f_{\#}$	5	0.32	0.44	Frequency dispersion of secondary patterns
Tapered	13	0.31	η_{opt}	3.9	0.63	0.70	Unfocused, high sidelobes in $\phi = 90$-cut. High cross-pol. in $\phi = 45$-cut
Tapered	7	0.31	$2\lambda f_{\#}$	5	0.54	0.61	Unfocused, high sidelobes in $\phi = 90$-cut. High cross-pol. in $\phi = 45$-cut.
Tapered airgap	14	0.31	η_{opt}	3.7	0.69	0.74	Unfocused, high sidelobes in $\phi = 90$-cut.
Tapered airgap	6	0.31	$2\lambda f_{\#}$	5	0.55	0.63	Unfocused, high sidelobes in $\phi = 90$-cut.

Chapter 9: Wideband antenna design conclusion

In this Part it has been shown through a preliminary parametric analysis that 1:3 bandwidth, frequency-stable illumination of a large $f_{\#} \geq 3.7$ reflector is possible using a tapered leaky slot under an extended hemispherical lens. An optical efficiency higher than 69% is possible using a lens with a radius $R = 14\ \mathrm{mm}$ and normalized extension length $L/R = 0.31$. There is a modest improvement (5%) in optical efficiency at the central frequency, $480\ \mathrm{GHz}$ and a 7% improvement at the highest frequency, $720\ \mathrm{GHz}$, compared to a tapered leaky slot under an optimized extended hemispherical lens (Fig. 8.9a).

To achieve $2\lambda f_{\#}$ sampling of the focal plane, three alternative lens antennas were evaluated. The considered straight leaky slot under a synthesized elliptical lens shows large variation of optical efficiency with frequency and has low optical efficiency, $\eta_{\text{opt}} = 0.44$, at its peak. This limits its usability if the goal is constant optical efficiency at a reflector. However, it is possible by using a tapered leaky slot to achieve optical efficiencies between $\eta_{\text{opt}} = 0.54 - 0.61$. By using a tapered leaky slot with a tapered airgap it is possible to get to $\eta_{\text{opt}} = 0.55 - 0.63$ (Fig. 8.9b). In all of these cases the $2\lambda f_{\#}$ sampling requirement is fulfilled.

The front-to-back efficiency of the tapered slot with tapered airgap is slightly higher than the regular tapered slot. The reflection efficiency of all considered lens antennas was calculated assuming a single quarter-wavelength matching layer (Tables 7.I to 7.III). These reflections are the primary cause of frequency variation in the realized aperture efficiencies (Figs. 8.9a and 8.9b). To reduce the frequency variation of the reflection efficiency, one could investigate wideband matching layer solutions such as grooved matching layers [39] or multi-shell lenses [32]. An additional benefit to a better matching layer is that the sidelobe level is reduced significantly [47], which could improve optical efficiency as well.

Appendix A: Phase center

The phase center of an antenna is the point from which far-field radiation appears to originate; i.e. the point from which, when looking in the far field, the phase over a sphere is constant is constant. For practical antennas, such a point may not exist or may vary with frequency. Nevertheless, for quasi-optical applications it is still useful to calculate an approximate phase center so that, for example, the approximate phase center of the antenna can be placed in the focus of a reflector. In this way, the phase error on the reflector can be minimized.

To calculate the phase center, the phase error loss over a sphere is minimized. The phase error loss is calculated using a formula adapted from [48]:

$$\mathrm{PEL} = \frac{|\int\int_{\Omega_0} E_{\mathrm{co}} \sin\theta \,\mathrm{d}\theta \,\mathrm{d}\phi|^2}{\int\int_{\Omega_0} |E_{\mathrm{co}}|^2 \sin\theta \,\mathrm{d}\theta \,\mathrm{d}\phi} \tag{A.1}$$

where Ω_0 is solid angle over which the integral is evaluated. Unless explicitly stated, this work will define Ω_0 to be region from broadside to where the field level is -10 dB over $\phi \in [0, 2\pi]$. Note that only the co-polarized component of the field is taken into account, the cross-polarization forms a different loss.

The routine minimizes the PEL by varying the reference point from which the far field is calculated. For structures symmetric in $\hat{\boldsymbol{x}}$ and $\hat{\boldsymbol{y}}$, the phase center is expected to lie along the $\hat{\boldsymbol{z}}$ axis, for which it can be shown that a displacement Δz of the reference system in the positive $\hat{\boldsymbol{z}}$-direction, the shifted electric field is:

$$\boldsymbol{E}^{\mathrm{shifted}} = \boldsymbol{E} \exp(-jk \cos\theta \Delta z) \tag{A.2}$$

as long as the shift is small compared to the original far-field distance.

The routine then calculates

$$\min_z \mathrm{PEL} = \min_z \frac{|\int\int_{\Omega_0} E_{\mathrm{co}}^{\mathrm{shifted}} \sin\theta \,\mathrm{d}\theta \,\mathrm{d}\phi|^2}{\int\int_{\Omega_0} |E_{\mathrm{co}}^{\mathrm{shifted}}|^2 \sin\theta \,\mathrm{d}\theta \,\mathrm{d}\phi} \tag{A.3}$$

Appendix B: Efficiencies

In this Appendix, definitions of various efficiencies are given.

The radiation efficiency of an antenna is defined here as the ratio of power in the far-field region of the antenna to the power accepted into the antenna's terminal.

$$\eta_{\text{rad}} = \frac{P_{\text{FF}}}{P_{\text{acc}}} \tag{B.1}$$

For lens antennas it is useful to factor the radiation efficiency into the front-to-back efficiency and reflection efficiency:

$$\eta_{\text{rad}} = \eta_{\text{F2B}}\eta_{\text{refl.}} \tag{B.2}$$

The spill-over efficiency is the fraction of total power intercepted by an optical component.

$$\eta_{\text{so}} = \frac{\int_{\Omega} |E|^2 \, \mathrm{d}\Omega}{\int_0^{2\pi} \int_0^{\pi} |E|^2 \sin\theta \, \mathrm{d}\theta \, \mathrm{d}\phi} \tag{B.3}$$

For a general reflector, Ω is the subtended solid angle of the reflector with respect to the feed. For the analysis in Chapter 7, Ω is the solid angle Ω inside the cut-off angle ($|\theta| \leq \theta_{\text{co}}$) of the leaky-slot antenna.

The taper efficiency is the ratio between the achieved directivity of an antenna to the maximum directivity of an aperture of the same size.

$$\eta_{\text{t}} = \frac{D_{\text{achieved}}}{D_{\text{max}}} \tag{B.4}$$

For a circular aperture of diameter D, the maximum directivity is $D_{\text{max}} = \left(\frac{\pi D}{\lambda}\right)^2$. For the leaky-lens analysis in Chapter 7, the taper efficiency is calculated over the solid angle Ω inside the cut-off angle ($|\theta| \leq \theta_{\text{co}}$) of the antenna's radiation pattern. The cut-off angle is chosen such that the optical efficiency in Eq. (B.6) is maximized. This maximization procedure is

explained in Chapter 7. The taper efficiency in Chapter 8 is calculated from the far-fields of the parabolas, where Ω is the upper hemisphere of the reflectors radiation pattern. For both cases, the following formula is used:

$$\eta_{\mathrm{t}} = \frac{\left|\int_{\Omega} E_{\mathrm{co}}\,\mathrm{d}\Omega\right|^2}{2\pi\,(1-\cos\theta_{\mathrm{max}})\int_{\Omega}|E_{\mathrm{co}}|^2\,\mathrm{d}\Omega} \tag{B.5}$$

where θ_{max} is the largest angle θ.

The optical efficiency measures how well a reflector is illuminated and is the product of the spill-over and the taper efficiency:

$$\eta_{\mathrm{opt}} = \eta_t \eta_{\mathrm{so}} \tag{B.6}$$

The aperture efficiency is the ratio of the gain achieved by an antenna (or reflector) to the maximum directivity of an aperture of the same size.

$$\eta_{\mathrm{ap}} = \frac{G_{\mathrm{achieved}}}{D_{\mathrm{max}}} \tag{B.7}$$

The achieved gain is the product of the directivity and the antenna efficiency. Equivalently, the aperture efficiency can be defined as the product of the radiation and the optical efficiencies:

$$\eta_{\mathrm{ap}} = \eta_{\mathrm{rad}}\eta_{\mathrm{opt}} \tag{B.8}$$

The Gaussicity, or Gaussian coupling efficiency, is a measure for the correlation between a Gaussian beam $\boldsymbol{E}_g$ and a beam under interest $\boldsymbol{E}_1$ [49]:

$$C_g = \frac{|\int_{\Omega_1}(\hat{\boldsymbol{i}}_{\mathrm{co}}\cdot\boldsymbol{E}_1)(\hat{\boldsymbol{i}}_{\mathrm{co}}\cdot\boldsymbol{E}_g)\,\mathrm{d}\Omega_1|^2}{\int_{\Omega}|\boldsymbol{E}_1|^2\,\mathrm{d}\Omega\int_{\Omega}|\boldsymbol{E}_2|^2\,\mathrm{d}\Omega} \tag{B.9}$$

where Ω is the upper hemisphere and Ω_1 is the cone over which the matching is calculated.

The Strehl ratio used in this thesis is calculated by Zemax [37]. The Strehl ratio is essentially a phase efficiency.

Appendix C: Field lens

The shape of the field lens is defined according to the definitions used in [37]. The optical axis is $\hat{\boldsymbol{z}}$ and the field lens lies in the xy-plane. The field lens has rotational symmetry around $\hat{\boldsymbol{z}}$. The z-component of the field lens shape is given by:

$$z = \frac{cr^2}{1 + \sqrt{1 - (1+k)c^2r^2}} \tag{C.1}$$

where $c = 1/R$ is the reciprocal of the radius of curvature, $r = \sqrt{x^2 + y^2}$ is the radial distance from the z-axis and $k = -e^2$ the conic constant, a function of the eccentricity.

Appendix D: Modified Dragonian reflector

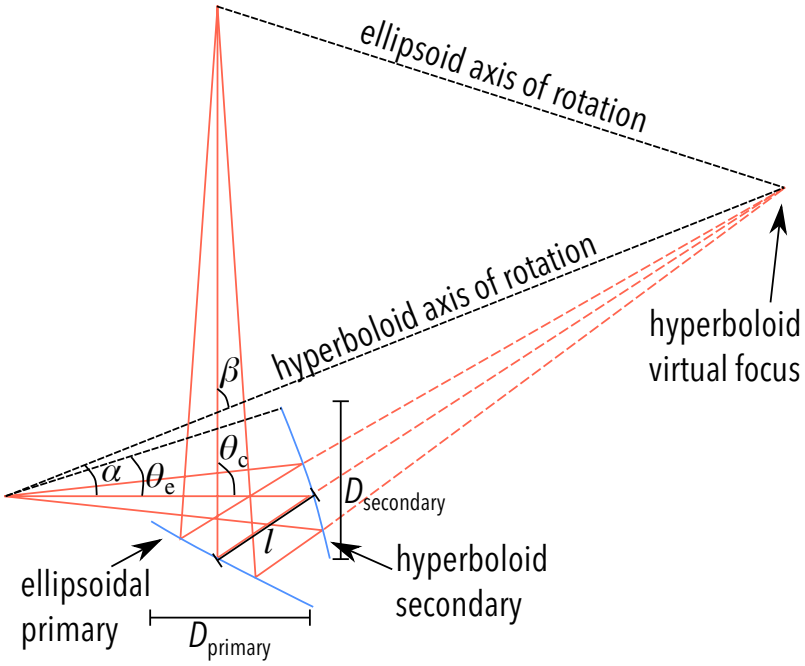

Fig. D.1. Ray picture of the modified Dragonian system with annotated geometry.

The classical Dragonian system [41] is a dual-reflector setup through which rays emerging from one point are focused at infinity through a hyperboloid secondary and parabolic primary mirror with zero geometrical-optics cross-polarization and minimal spillover [46]. The modified Dragonian system is shown in Fig. D.1, where the same geometric parameters are used as in [46], the difference being the paraboloid primary mirror is interchanged for an ellipsoidal primary to focus the exiting rays at a real point [33]. The angle between central ray incident on the secondary reflector and the hyperboloid axis of rotation is called α, while the angle between the central ray exiting the ellipsoidal primary is called β. The sum $\theta_c = \alpha + \beta$

is thus the angle between the incident and exiting central rays. The angle subtended by the hyperboloid secondary to the feed is called θ_e. The centers of the reflectors are separated by a distance l.

The operating principle of a Dragonian system is to place a hyperboloid subreflector with the input Gaussian beam waist position at one of its foci. The rays reflected from the hyperboloid will then appear to originate from a virtual focus: the second focus of the hyperboloid. This is the first magnification, $\mathcal{M}_{\text{hyp}}$. The ellipsoid is then constructed such that it has one of its foci at this virtual focus and the other at the desired output focal point. This causes another magnification determined by the ratio of the two focal lengths of the ellipsoid: $\mathcal{M}_{\text{ell}} = f_1/f_2$. Most importantly for this scenario, the total magnification $\mathcal{M} = \mathcal{M}_{\text{hyp}}\mathcal{M}_{\text{ell}}$ can be controlled both by shaping the reflectors and by displacing them.

Appendix E: Dielectric lens types

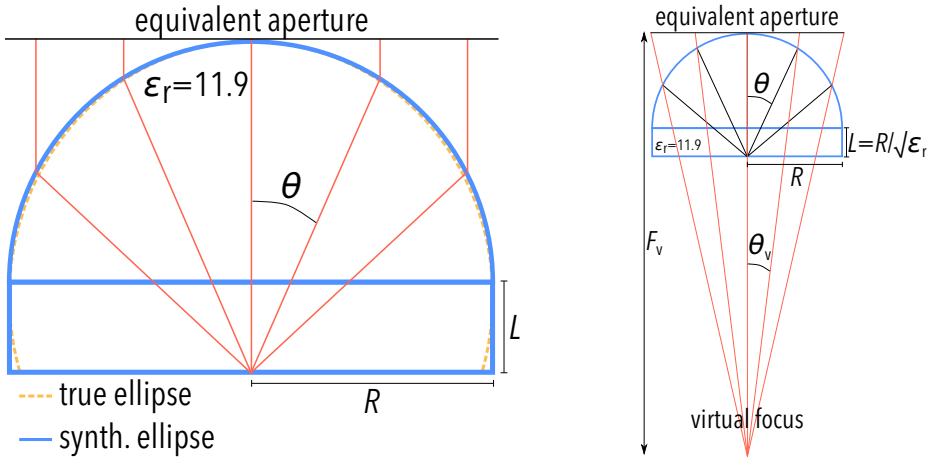

Fig. E.1. Ray-trace cross-sections of (a) the synthesized elliptical lens and (b) the hyper-hemispherical lens.

E.1 Synthesized elliptical lens

A silicon synthesized elliptical lens has an extension length between $L/R = 0.36$ and $L/R = 0.39$ depending on the lens radius [38]. Such a synthesized ellipse will then collimate rays originating from the lower focus of the synthesized ellipse. However, since the phase center of a leaky slot is below the ground plane, the extension must be shortened to compensate for this phase center. A ray-trace cross-section of this lens type is shown schematically in Fig. E.1a. The elliptical lens operation is diffraction-limited and therefore has an intrinsic frequency variation in its radiation pattern, even if the fields inside the lens do not.

E.2 Hyper-hemispherical lens

A hyper-hemispherical lens has an extension length $L = R/\sqrt{\epsilon_r}$ [38] which creates a virtual focus below the ground plane for rays emerging at the antenna. This is shown in Fig. E.1b. The phase of the rays on the equivalent aperture relative to the central ray is then quadratic: $\psi = k\rho^2/2F_v$, with $F_v = R(\sqrt{\epsilon_r}+1)$ the distance from the equivalent aperture to the virtual focus, ρ the radial displacement in the aperture plane and k the free-space wavenumber. Such a quadratic phase leads to a widening of the beams [50]. Furthermore, this quadratic phase variation is linear with frequency due to the $k = 2\pi/\lambda$ term in the expression. The hypothesis is that the linear phase variation in frequency offsets the linear increase in directivity of the lens antenna such that the secondary patterns are constant in frequency.

The radius R of the hyper-hemisphere is a trade-off. If the lens is taken too small, the ray-picture of Fig. E.1 is no longer valid due to diffraction effects. On the other hand, for very large lenses the ray-picture of Fig. E.1 is almost exact. This implies that the secondary pattern is a compressed version of the primary pattern with θ replaced by $\theta_v = \arcsin(\frac{L}{R}\sin\theta)$. In the case of the leaky slot this is not desirable due to the low power radiated towards broadside in the primary patterns. Therefore, a trade-off in the lens radius must be found between geometrical limit and the diffraction limit.

As with the elliptical lens, the extension must be corrected for the phase center of the leaky slot.

Appendix F: Publications

I have contributed to the following scientific publications during the course of this thesis work:

1. A. Endo, D. Thoen, K. Karatsu, N van Marrewijk, S. Bosma, O. Yurduseven, N. Llombart, M. Naruse, N. Tomita, J. Suzuki, A. Taniguchi, K. Kohno, S. Ishii, J. Maekawa, R. Kawabe, T. Oshima, K. Chin, Y. Tamura, T. Takekoshi, K. Fujita, S. Nakatsubo, T. Klapwijk, P. van der Werf, S. Yates, A. Baryshev, V. Murugesan, R. Huiting, J. Bueno and J. Baselmans, *Development of 'DESHIMA on ASTE': towards a field test of a submillimeter wave superconducting on-chip filterbank spectrometer based on kinetic inductance detectors*, 17th International Workshop on Low Temperature Detectors (LTD17), July 17-21st, Kurume City, Japan.
2. O. Yurduseven, S. Bosma, A. Endo, and N. Llombart Juan, *A Wideband Leaky Lens Antenna with Frequency-Stable Beams for DESHIMA Spectrometer*, 42nd International Conference on Infrared, Millimeter and Terahertz Waves (IRMMW-THz), *accepted*, August 27th-September 1st, Cancún, México.

References

[1] C. M. Casey, D. Narayanan, and A. Cooray, "Dusty star-forming galaxies at high redshift", *Physics Reports*, vol. 541, no. 2, pp. 45–161, 2014, ISSN: 03701573. DOI: 10.1016/j.physrep.2014.02.009. arXiv: 1402.1456. [Online]. Available: http://dx.doi.org/10.1016/j.physrep.2014.02.009.

[2] A. Endo, "Superconducting on-chip spectrometery for millimeter-submillimeter wave astronomy", *IEICE Trans. Electron.*, vol. E98-C, no. 3, pp. 219–226, 2015, ISSN: 17451353. DOI: 10.1587/transele.E98.C.219.

[3] W. S. Holland, D. Bintley, E. L. Chapin, *et al.*, "Scuba-2: the 10 000 pixel bolometer camera on the james clerk maxwell telescope", *Monthly Notices of the Royal Astronomical Society*, vol. 430, no. 4, pp. 2513–2533, 2013, ISSN: 00358711. DOI: 10.1093/mnras/sts612. arXiv: 1301.3650.

[4] A. M. Baryshev, J. J. A. Baselmans, S. J. C. Yates, *et al.*, "Large format antenna coupled micorwave kinetic iinductance detector arrays for radioastronomy", *International Conference on Infrared, Millimeter, and Terahertz Waves, IRMMW-THz*, vol. 95, no. 20, p. 42 504, 2014, ISSN: 21622035. DOI: 10.1109/IRMMW-THz.2014.6956150.

[5] J. D. Vieira, D. P. Marrone, S. C. Chapman, *et al.*, "Dusty starburst galaxies in the early universe as revealed by gravitational lensing", *Nature*, vol. 495, no. 7441, pp. 344–347, 2013, ISSN: 0028-0836. DOI: 10.1038/nature12001. arXiv: 1303.2723. [Online]. Available: http://www.nature.com/doifinder/10.1038/nature12001.

[6] A. Endo, J. J. A. Baselmans, P. P. van der Werf, *et al.*, "Development of deshima: a redshift machine based on a superconducting on-chip filterbank", *Proc. of SPIE*, vol. 8452, pp. 84520X–84520X–15, 2012, ISSN: 0277786X. DOI: 10.1117/12.925637.

[7] C. Carilli and R. Wang, "Co line width differences in early universe molecular emission-line galaxies: submillimeter galaxies versus qso hosts", *The Astronomical Journal*, vol. 131, no. 6, p. 2763, 2006, ISSN: 0004-6256. DOI: 10.1086/503872. [Online]. Available: http://iopscience.iop.org/1538-3881/131/6/2763.

[8] Kotaro Kohno, "The atacama submillimeter telescope experiment (aste)", *Proceedings of SPIE*, vol. 5489, no. August 2003, pp. 763–772, 2004, ISSN: 0277786X. DOI: 10.1117/12.551391. [Online]. Available: http://link.aip.org/link/?PSI/5489/763/1{\&}Agg=doi.

[9] A. Neto, "Uwb, non dispersive radiation from the planarly fed leaky lens antenna part 1: theory and design", *IEEE Transactions on Antennas and Propagation*, vol. 58, no. 7, pp. 2238–2247, 2010, ISSN: 0018926X. DOI: 10.1109/TAP.2010.2048879.

[10] P. K. Day, H. G. LeDuc, B. A. Mazin, *et al.*, "A broadband superconducting detector suitable for use in large arrays", *Nature*, vol. 425, no. 6960, pp. 817–821, 2003, ISSN: 0028-0836. DOI: 10.1038/nature02037. [Online]. Available: http://www.nature.com/doifinder/10.1038/nature02037.

[11] J. van Rantwijk, M. Grim, D. van Loon, *et al.*, "Multiplexed readout for 1000-pixel arrays of microwave kinetic inductance detectors", *IEEE Transactions on Microwave Theory and Techniques*, vol. 64, no. 6, pp. 1876–1883, 2016, ISSN: 0018-9480. DOI: 10.1109/TMTT.2016.2544303. [Online]. Available: http://ieeexplore.ieee.org/document/7445881/.

[12] D. J. Thoen, B. G. C. Bos, E. A. F. Haalebos, *et al.*, "Superconducting nbtin thin films with highly uniform properties over a 100 mm wafer", *IEEE Transactions on Applied Superconductivity*, vol. 27, no. 4, pp. 1–5, 2017, ISSN: 1051-8223. DOI: 10.1109/TASC.2016.2631948. arXiv: 1609.01526. [Online]. Available: http://ieeexplore.ieee.org/document/7752837/.

[13] A. Neto, N. Llombart, J. J. A. Baselmans, *et al.*, "Demonstration of the leaky lens antenna at submillimeter wavelengths", *IEEE Transactions on Terahertz Science and Technology*, vol. 4, no. 1, pp. 26–32, 2014, ISSN: 2156342X. DOI: 10.1109/TTHZ.2013.2284553.

[14] A. Baryshev, J. J. A. Baselmans, A. Freni, *et al.*, "Progress in antenna coupled kinetic inductance detectors", *IEEE Transactions on Terahertz Science and Technology*, vol. 1, no. 1, pp. 112–123, 2011, ISSN: 2156342X. DOI: 10.1109/TTHZ.2011.2159532.

[15] J. Bueno, O. Yurduseven, S. J. C. Yates, *et al.*, "Photon noise limited performance over an octave of bandwidth of kinetic inductance detectors for sub-millimeter astronomy", *International Conference on Infrared, Millimeter, and Terahertz Waves, IRMMW-THz*, vol. 2016-Novem, pp. 1–2, 2016, ISSN: 21622035. DOI: 10.1109/IRMMW-THz.2016.7758429.

[16] A. Endo, S. J. C. Yates, J. Bueno, *et al.*, "Superconducting coplanar waveguide filters for submillimeter wave on-chip filterbank spectrometers", *Journal of Low Temperature Physics*, vol. 184, no. 1-2, pp. 412–417, 2016, ISSN: 15737357. DOI: 10.1007/s10909-016-1579-8.

[17] S. Hailey-Dunsheath, E. Shirokoff, P. S. Barry, *et al.*, "Status of superspec: a broadband, on-chip millimeter-wave spectrometer", W. S. Holland and J. Zmuidzinas, Eds., vol. 9153, 2014, p. 91530M. DOI: 10.1117/12.2057229. [Online]. Available: http://proceedings.spiedigitallibrary.org/proceeding.aspx?doi=10.1117/12.2057229.

[18] G. Cataldo, W.-T. Hsieh, W.-C. Huang, *et al.*, "Micro-spec: an ultracompact, high-sensitivity spectrometer for far-infrared and submillimeter astronomy", *Applied Optics*, vol. 53, no. 6, p. 1094, 2014, ISSN: 0003-6935. DOI: 10.1364/AO.53.001094. [Online]. Available: http://ao.osa.org/abstract.cfm?URI=ao-53-6-1094https://www.osapublishing.org/abstract.cfm?URI=ao-53-6-1094.

[19] T. S. Chu, "An imaging beam waveguide feed", *IEEE Transactions on Antennas and Propagation*, vol. 31, no. 4, pp. 614–619, 1983, ISSN: 15582221. DOI: 10.1109/TAP.1983.1143090.

[20] S. Paine, D. C. Papa, R. L. Leombruno, *et al.*, "Beam waveguide and receiver optics for the sma", *Fifth International Symposium on Space Terahertz Technology*, pp. 811–823, 1994. [Online]. Available: http://web.eecs.umich.edu/{~}jeast/paine{_}1994{_}12{_}6.pdf.

[21] Y.-c. Chou and C.-t. Li, "Array receiver optics design for the submillimeter array", in *24th International Symposium on Space Terahertz Technology*, Groningen, the Netherlands, 2013, pp. 1–7. [Online]. Available: http://ir.sinica.edu.tw/handle/201000000A/75580.

[22] P. F. Goldsmith, *Quasioptical Systems: Gaussian Beam Quasioptical Propogation and Applications*. New York: IEEE Press, 1998, p. 412, ISBN: 0-7803-3439-6. [Online]. Available: http://ieeexplore.ieee.org/xpl/bkabstractplus.jsp?bkn=5264471.

[23] P. Gibson, "The vivaldi aerial", in *9th European Microwave Conference*, Brighton, United Kingdom: IEEE, 1979, pp. 101–105. DOI: 10.1109/EUMA.1979.332681.

[24] M. V. Ivashina, M. N. M. Kehn, P. S. Kildal, *et al.*, "Decoupling efficiency of a wideband vivaldi focal plane array feeding a reflector antenna", *IEEE Transactions on Antennas and Propagation*, vol. 57, no. 2, pp. 373–382, 2009, ISSN: 0018926X. DOI: 10.1109/TAP.2008.2011184.

[25] R. Olsson, P. S. Kildal, and S. Weinreb, "The eleven antenna: a compact low-profile decade bandwidth dual polarized feed for reflector antennas", *IEEE Transactions on Antennas and Propagation*, vol. 54, no. 2, pp. 368–375, 2006, ISSN: 0018926X. DOI: 10.1109/TAP.2005.863392.

[26] J. Teniente, R. Gonzalo, and C. Del-Río, "Ultra-wide band corrugated gaussian profiled horn antenna design", *IEEE Microwave and Wireless Components Letters*, vol. 12, no. 1, pp. 20–21, 2002, ISSN: 15311309. DOI: 10.1109/7260.975722.

[27] P Yagoubov, A Gonzalez, V Tapia, *et al.*, "67-116 ghz optics development for alma band 2-3 receivers", in *41st International Conference on Infrared, Millimeter, and Terahertz waves (IRMMW-THz)2*, Copenhagen, Denmark, 2016, pp. 4–5. DOI: 10.1109/IRMMW-THz.2016.7758971.

[28] C. Granet, R. Bolton, and G. Moorey, "A smooth-walled spline-profile horn as an alternative to the corrugated horn for wide band millimeter-wave applications", *IEEE Transactions on Antennas and Propagation*, vol. 52, no. 3, pp. 848–854, 2004, ISSN: 0018926X. DOI: 10.1109/TAP.2004.825156.

[29] A. Akgiray, S. Weinreb, W. A. Imbriale, *et al.*, "Circular quadruple-ridged flared horn achieving near-constant beamwidth over multioctave bandwidth: design and measurements", *IEEE Transactions on Antennas and Propagation*, vol. 61, no. 3, pp. 1099–1108, 2013, ISSN: 0018926X. DOI: 10.1109/TAP.2012.2229953.

[30] A Gonzalez, K Kaneko, and S Asayama, "Recent work on (sub-)mm-wave ultra wideband corrugated horns for radio astronomy", in *11th European Conference on Antennas and Propagation (EUCAP)*, 2017, pp. 3327–3331, ISBN: 9788890701870.

[31] O. Yurduseven, D. Cavallo, and A. Neto, "Wideband dielectric lens antenna with stable radiation patterns fed by coherent array of connected leaky slots", *IEEE Transactions on Antennas and Propagation*, vol. 62, no. 4, pp. 1895–1902, 2014, ISSN: 0018926X. DOI: 10.1109/TAP.2014.2298875.

[32] C. A. Fernandes, E. B. Lima, and J. R. Costa, "Broadband integrated lens for illuminating reflector antenna with constant aperture efficiency", *IEEE Transactions on Antennas and Propagation*, vol. 58, no. 12, pp. 3805–3813, 2010, ISSN: 0018926X. DOI: 10.1109/TAP.2010.2078463.

[33] G. Chattopadhyay, A. Freni, N. Llombart, *et al.*, *Handbook of Reflector Antennas and Feed Systems Vol. III: Applications of Reflectors*, 1st ed., S. Rao, L. Shafai, and S. Satish, Eds. Boston: Artech House, 2013, pp. 145–213, ISBN: 9781608075195.

[34] S. J. C. Yates, *Private communication*, 2017.

[35] CST Computer Simulation Technology AG, *Cst microwave studio - 3d em simulation software*, 2016. [Online]. Available: https://www.cst.com/products/cstmws.

[36] TICRA, *Grasp | ticra*. [Online]. Available: https://www.ticra.com/products/software/grasp.

[37] Zemax, *Opticstudio - zemax*. [Online]. Available: http://www.zemax.com/os/opticstudio.

[38] D. F. Filipovic, S. S. Gearhart, and G. M. Rebeiz, "Double-slot antennas on extended hemispherical and elliptical silicon dielectric lenses", *IEEE Transactions on Microwave Theory and Techniques*, vol. 41, no. 10, pp. 1738–1749, 1993, ISSN: 15579670. DOI: 10.1109/22.247919.

[39] O. Yurduseven, "Wideband integrated lens antennas for terahertz deep space investigation", PhD thesis, Delft University of Technology, 2016. DOI: 10.4233/uuid:f30b8bca-173f-4a13-b545-e18e137c9fc6. [Online]. Available: http://repository.tudelft.nl/islandora/object/uuid{\%}3Af30b8bca-173f-4a13-b545-e18e137c9fc6?collection=research.

[40] C. A. Balanis, *Antenna Theory Analysis and Design*, 3. 2005, p. 1136, ISBN: 9786468600. DOI: 10.1049/ep.1982.0113.

[41] C. Dragone, "Unique reflector arrangement with very wide field of view for multibeam antennas", *Electronics Letters*, vol. 19, no. 25/26, pp. 1061–1062, 1983. DOI: 10.1049/el:19830720. [Online]. Available: http://ieeexplore.ieee.org/document/4248277/.

[42] T. S. Chu and R. H. Turrin, "Depolarization properties of offset reflector antennas", *IEEE Transactions on Antennas and Propagation*, vol. 21, no. 3, pp. 339–345, 1973, ISSN: 15582221. DOI: 10.1109/TAP.1973.1140479.

[43] J. Dijk, C. van Diepenbeek, E. Maanders, *et al.*, "The polarization losses of offset paraboloid antennas", *IEEE Transactions on Antennas and Propagation*, vol. 22, no. 4, pp. 513–520, 1974, ISSN: 0096-1973. DOI: 10.1109/TAP.1974.1140847. [Online]. Available: http://ieeexplore.ieee.org/document/1140847/.

[44] E. Gandini and N. Llombart, "Toward a real time stand-off submillimeter-wave imaging system with large field of view: quasi-optical system design considerations", in *Proceedings of SPIE*, D. A. Wikner and A. R. Luukanen, Eds., vol. 9462, 2015, p. 946 205. DOI: 10.1117/12.2177038. [Online]. Available: http://proceedings.spiedigitallibrary.org/proceeding.aspx?doi=10.1117/12.2177038.

[45] Y. Mizugutch, M. Akagawa, and H. Yokoi, "Offset dual reflector antenna", in *Antennas and Propagation Society International Symposium*, 1976, pp. 2–5. DOI: 10.1109/APS.1976.1147539. [Online]. Available: http://ieeexplore.ieee.org/document/1147539/.

[46] S. Chang and A. Prata, "The design of classical offset dragonian reflector antennas with circular apertures", *IEEE Transactions on Antennas and Propagation*, vol. 52, no. 1, pp. 12–19, 2004, ISSN: 0018926X. DOI: 10.1109/TAP.2003.822435.

[47] A. Neto, S. Monni, and F. Nennie, "Uwb, non dispersive radiation from the planarly fed leaky lens antenna part ii: demonstrators and measurements", *IEEE Transactions on Antennas and Propagation*, vol. 58, no. 7, pp. 2248–2258, 2010, ISSN: 0018-926X. DOI: 10.1109/TAP.2010.2048880. [Online]. Available: http://ieeexplore.ieee.org/document/5454312/.

[48] T. A. Milligan, *Modern antenna design*, 2nd ed. Hoboken, N.J.: IEEE Press, 2005, ISBN: 9780471457763.

[49] S. E. Schwarz, "Efficiency of quasi-optical couplers", *International Journal of Infrared and Millimeter Waves*, vol. 5, no. 12, pp. 1517–1525, 1984, ISSN: 0195-9271. DOI: 10.1007/BF01040503. [Online]. Available: http://link.springer.com/10.1007/BF01040503.

[50] A. Love, "Quadratic phase error loss in circular apertures", *Electronics Letters*, vol. 15, no. 10, p. 276, 1979, ISSN: 00135194. DOI: 10.1049/el:19790196. [Online]. Available: http://digital-library.theiet.org/content/journals/10.1049/el{_}19790196.